ANIMAL LOCOMOTION

Emergence of robust self-organized undulatory swimming based on local hydrodynamic force sensing

Robin Thandiackal[1,2*†], Kamilo Melo[1,3*†], Laura Paez[1], Johann Herault[4], Takeshi Kano[5], Kyoichi Akiyama[5], Frédéric Boyer[4], Dimitri Ryczko[6], Akio Ishiguro[5], Auke J. Ijspeert[1*]

Undulatory swimming represents an ideal behavior to investigate locomotion control and the role of the underlying central and peripheral components in the spinal cord. Many vertebrate swimmers have central pattern generators and local pressure-sensitive receptors that provide information about the surrounding fluid. However, it remains difficult to study experimentally how these sensors influence motor commands in these animals. Here, using a specifically designed robot that captures the essential components of the animal neuromechanical system and using simulations, we tested the hypothesis that sensed hydrodynamic pressure forces can entrain body actuation through local feedback loops. We found evidence that this peripheral mechanism leads to self-organized undulatory swimming by providing intersegmental coordination and body oscillations. Swimming can be redundantly induced by central mechanisms, and we show that, therefore, a combination of both central and peripheral mechanisms offers a higher robustness against neural disruptions than any of them alone, which potentially explains how some vertebrates retain locomotor capabilities after spinal cord lesions. These results broaden our understanding of animal locomotion and expand our knowledge for the design of robust and modular robots that physically interact with the environment.

INTRODUCTION

Locomotion in vertebrate animals is due to an interplay of the central nervous system (the brain and the spinal cord), the peripheral nervous system (nerves projecting to muscles and sensory neurons), the musculoskeletal system, and the environment. The interactions between the central and peripheral nervous systems are complex. In particular, the discussion of central (feedforward) versus peripheral (feedback) locomotion control represents an old and fundamental debate in animal locomotion started by Graham-Brown and Sherrington (*1*) and constitutes an important trade-off in control engineering (*2*). Whereas Sherrington supported the idea that locomotion is due to a chain of rhythmic reflexes (peripheral mechanism), Graham-Brown made his case for locomotion due to neural rhythm generators (central mechanism). This debate has turned in favor of Graham-Brown with the discovery of central pattern generators (CPGs), which are networks of rhythmogenic neural circuits (i.e., oscillators) that can generate coordinated activity when isolated from sensory feedback and descending drive from invertebrates (*3*) to vertebrates, including mammals (*4*, *5*). A general view is that CPGs offer the basic patterns of locomotion by providing rhythm generation and coordination and that sensory feedback modulates these patterns to adapt to the environment. However, an intriguing systematic observation made from invertebrates to mammals is that, when the CPGs are activated but generate no movement and therefore receive no sensory feedback ("fictive motor activity"), the frequency of motor activity is much slower (2 to 10 times) [e.g., leech (*6*), lamprey (*7*), salamander (*8*), and mouse (*9*)]. Another remarkable observation is the high robustness of some undulatory swimmers, such as eels or lampreys, which can maintain swimming performance despite acute, full transections of the spinal cord at midbody level, i.e., with a major disruption of the CPG (*10*, *11*). In other vertebrates, full transections indeed lead to major disruptions of locomotor behaviors with either no rhythmic activity below lesion or rhythmic activity that is not coordinated above and below lesion. These observations in undulatory swimmers suggest that sensory feedback can play a role not only in pattern modulation but also in the generation of coordinated rhythms between different parts of the spinal cord.

Studies in vertebrate undulatory swimmers have contributed a great deal to our understanding of the interplay between sensory feedback and CPGs. As such, one type of feedback has been identified in the mechanosensory edge cells that convey proprioceptive information in lamprey. These cells respond to spinal cord stretching and participate in motor burst termination by exciting ipsilateral segmental neurons and inhibiting the contralateral ones (*12*–*15*). As a result, edge cells can entrain CPG activity and contribute to rhythm coordination (*16*, *17*).

In contrast to the more explored proprioception, past work has also identified cells relaying movement-related exteroceptive feedback to local segmental motor circuits. Such sensory feedback is provided by mechanoreceptor cells that are sensitive to touch and pressure and thus provide information about the hydrodynamic forces applied locally on the body. In lampreys, for instance, such mechanoreceptors are called dorsal cells and have been found to be sensitive to touch and pressure on the lateral side of the body (*18*, *19*). The corresponding cell bodies that are located in the dorsal part of the spinal cord have their receptive fields on the lateral parts of the body (*18*). Buchanan and Cohen (*20*) further demonstrated that stimulated dorsal cells provide excitation ipsilaterally to the local segmental motor circuits and inhibition to the contralateral ones (*20*) and therefore highlighted the presence of sensory feedback loops based on exteroception. However, because it is difficult to specifically manipulate these intricate sensory and motor cell populations, it remains elusive to what extent exteroceptive mechanoreceptor cells interact with rhythmogenic CPG circuits and how they

[1]École Polytechnique Fédérale de Lausanne (EPFL), Lausanne, Switzerland. [2]Harvard University, Cambridge MA, USA. [3]KM-RoBoTa Sàrl, Renens, Switzerland. [4]LS2N, IMT Atlantique, Nantes, France. [5]Tohoku University, Sendai, Japan. [6]Université de Sherbrooke, Sherbrooke, Canada.
*Corresponding author. Email: rthandiackal@fas.harvard.edu (R.T.); kamilo.melo@epfl.ch (K.M.); auke.ijspeert@epfl.ch (A.J.I.)
†These authors contributed equally to this work.

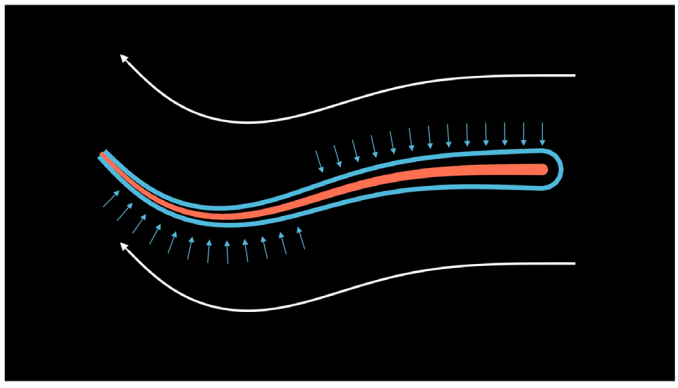

Movie 1. Motivation of this study and summary of the results.

contribute to rhythm coordination (like the edge cells) or if and how they contribute to rhythmogenesis (i.e., rhythm generation).

We addressed this open question in the present study using robotics and modeling, which offer the opportunity to compare the respective contribution of central and peripheral mechanisms in a behavior executed under controlled conditions (Movie 1). We focused on undulatory movements because (i) they are used by many aquatic species to generate thrust; (ii) their biological substrate is extensively studied in animal models (lamprey, zebrafish, *Xenopus* embryo, salamander, etc.); and (iii) they are of major interest in engineering studies aimed at designing propulsion systems for swimming robots. On the basis of the dorsal cell local projections and their modulation of muscle activation in lamprey (*20*), we hypothesized that these hydrodynamic force sensors form local sensory-motor loops with the capability to generate rhythmic swimming activity and coordinate body undulations, independently of the rhythmogenic ability of the segmental motor circuits. Note that we explore sensory feedback that projects directly to the spinal cord circuits, as opposed to the lateral line system, which projects to supraspinal centers and which therefore only indirectly modulates spinal cord activity through high-level speed and heading commands.

To test our hypothesis, we custom-designed a robot with dedicated distributed force-sensing modules and explored a model of the neural circuits that allowed us to incorporate CPGs as well as a specific exteroceptive force feedback mechanism. Following this approach, our key finding is that hydrodynamic force feedback is a powerful mechanism that contributes not only to motor pattern modulation but also to motor rhythm generation and coordination. It is therefore to a large extent redundant with the CPG function. In particular, we found that the hydrodynamic force feedback (i) increases the frequency of swimming movements; (ii) can coordinate uncoupled neural oscillators to generate forward swimming; (iii) can, in principle, generate rhythmic activity without the need for rhythmogenic neural oscillators; and (iv) provides redundancy such that control circuits that combine both central and peripheral components tend to be more robust against neural disruptions than any of these alone.

Biomechanics shapes locomotion

In their review *Spikes alone do not behavior make: Why neuroscience needs biomechanics*, Tytell *et al.* (*21*) underline the importance of the physics of muscles, bodies, and the real-world environment on shaping locomotor behavior by interacting with the neural control circuits. In our study, we followed an approach that integrates this aspect of the biomechanics by implementing and testing models of neural control circuits and sensory feedback loops on a specifically designed robot that provides the relevant physical interactions.

Robotics has been used to investigate locomotor function in a variety of different animals and substrates (*22*–*24*) and is particularly valuable to explore aquatic locomotion that results from complex body-fluid interactions. As a consequence, robotic fish models have shed new light on key biological and fluid mechanics aspects of animal swimming (*25*–*30*). In addition, a number of bioinspired undulatory swimming robots have been designed with engineering applications in mind (*31*–*41*). Testing our hypothesis of distributed force feedback loops for pattern generation required a robot that is able to both generate undulatory movements in water and incorporate distributed measurements of interaction forces with the water. Many of the existing swimming robots are primarily used to explore and exploit actuation and propulsive mechanisms, whereas only a few systems have incorporated fluid sensing. Robots with artificial lateral line and pressure sensing systems (*42*–*46*) have been designed for closed-loop control to achieve rheotaxis and station holding. These systems are based on measurements of pressures in localized points along the body and ultimately help to deduce flow speeds from pressure gradients around a swimming robot. However, the corresponding measurements of flow speed do not provide direct information about hydrodynamic interaction forces along the body, which are needed to investigate our proposed hypothesis. In general, distributed force feedback for undulatory swimming represents a sensor modality that has not been investigated with respect to motor rhythm generation and coordination, in part because of difficulties to adequately measure direct hydrodynamic forces on an undulatory swimming body. This motivated the design of our own robot together with the design of specific force-sensing modules for the purpose of this study.

MODELING

Neuromechanical model, robot, and simulation

Our neuromechanical model combines a sensorized viscoelastic body and a simplified spinal cord implemented as a distributed set of locally connected segmental circuits. We consider the body as a planar chain of rigid segments connected by actuated joints. At each joint (Fig. 1A), viscoelastic body deformation is induced by signals from the segmental circuit that coordinate the left-right alternated activations of a simulated pair of antagonist muscles (see Materials and Methods). Each local segmental circuit contributes to the local body deformation on the basis of the ability of each segment to sense the resulting lateral hydrodynamic forces acting on it. We built a lamprey-like robot, named AgnathaX (Fig. 1, B to D; Materials and Methods; and fig. S1A), that implements this neuromechanical model to evaluate its behavior in real body-fluid interactions. Unlike other undulatory swimming robots that can measure joint torques (*31*), which is a form of proprioceptive feedback (see Discussion), here, we designed an implementation of exteroceptive feedback. On the left and right sides of each segment, force plates sense the hydrodynamic forces. We used pairs of contralateral force plates on each segment to directly obtain the net lateral hydrodynamic force, which results from the difference of sensed left and right individually measured forces (each force plate can measure positive or negative values of the corresponding hydrodynamic force on its side independently).

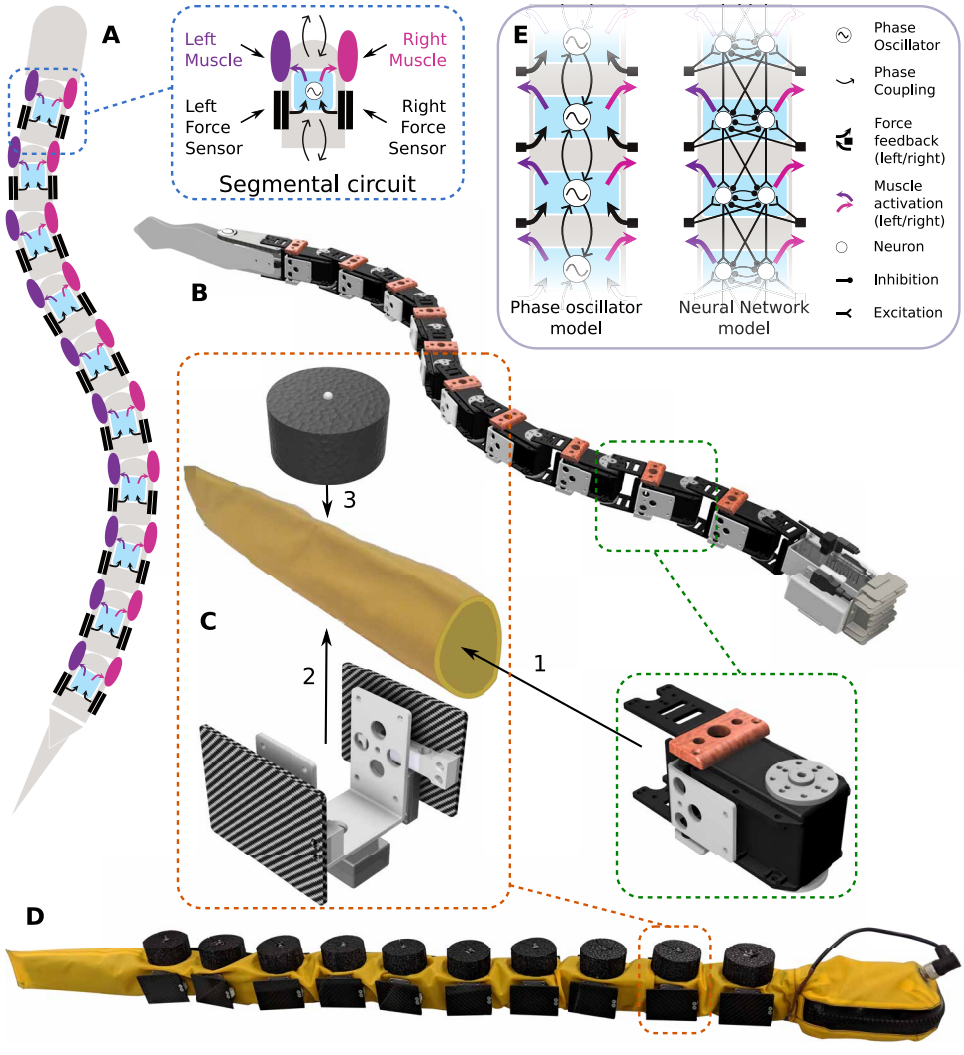

Fig. 1. Implementation of central and peripheral components for undulatory swimming in the robot. (**A**) Model composed of rigid body segments connected by actuated joints. Each segment (in detail) has its own circuit (with oscillators and couplings), left and right antagonistic muscles, and a pair of lateral force sensors. (**B**) Core of the robot AgnathaX composed of 10 servomotors (in detail), with a Linux computer, batteries, and a passive tail module. (**C**) Outer part of the robot AgnathaX showing its assembly sequence (in detail). (1) The robot core is introduced into a waterproof swim suit. (2) The force plate module (communication circuit, load cells with corresponding amplifiers and carbon fiber plates) is fixed from the outside by means of magnets. The modules are electrically interconnected (power and communication) to their neighbors and lastly connect to the robot head. (3) A floating element with an embedded LED for motion tracking is attached on top of each module. (**D**) Full assembly of the waterproofed robot AgnathaX with all the sensors and tracking lights. (**E**) Comparison between the phase oscillator model and the neural network model.

To investigate a variety of parameters and their effects, we also implemented the neuromechanical model in a simulation of the body that uses an analytic representation of the hydrodynamic forces based on an improved Lighthill model (*47*, *48*) including resistive drag and reactive forces (see Materials and Methods, fig. S1B, and table S1).

Design of the local feedback mechanism

Given the body model, we can formulate our hypothesis that local pressure sensation from lateral mechanoreceptor cells (such as the lamprey dorsal cells) forms local sensory-motor loops by proposing a simple feedback mechanism that is added to a CPG circuit. To design this feedback mechanism, we first quantified the relationship between body deformation and hydrodynamic forces during effective target swimming movements in a specific set of experiments with the robot and the simulated model. We tested two types of body deformations imposing traveling waves of body undulations with (i) a constant uniform amplitude and (ii) a linearly increasing amplitude gradient from head to tail along the anteroposterior body axis. These target swimming patterns were chosen because they produce fast swimming speeds similar to those observed in undulatory swimmers like lampreys. In addition, we varied the magnitude of the gradient and tested for a range of frequencies. Whereas body deformations in the rest of this study were imposed by torques from a muscle model, the body deformations (joint angle positions) here were rigidly prescribed by means of a proportional-derivative position controller (Materials and Methods). We used this control scheme to predefine exact deformations along the body of which we could analyze the measured hydrodynamic forces and their relation to those deformations for specific target swimming movements.

We used the phase lag between joint angles and local hydrodynamic force as a proxy to quantify the timing between body deformation and forces. The distribution of phase lags between joint angles and forces along the body as well as examples of forces acting on the body depending on its bending during rigidly prescribed steady swimming are presented in Fig. 2. We found that these phase lags were small (simulation with constant amplitude, −1.10 ± 4.20%; simulation with gradient amplitude,−1.60 ± 3.39%; robot with constant amplitude, −10.14 ± 9.28%; robot with gradient amplitude, −8.39 ± 6.50%) within the tested conditions; thus, local body deformation and hydrodynamic forces are nearly in phase, with peaks of hydrodynamic forces arriving slightly before peaks of deformations.

Motivated by this local phase locking, we therefore propose a mechanism that entrains the actuator activation that drives body deformation by constantly modifying its timing depending on the measured force signal. We implemented this mechanism in a system represented by Eqs. 1 to 3 that describes the dynamics of the local activation u_n in a segmental circuit

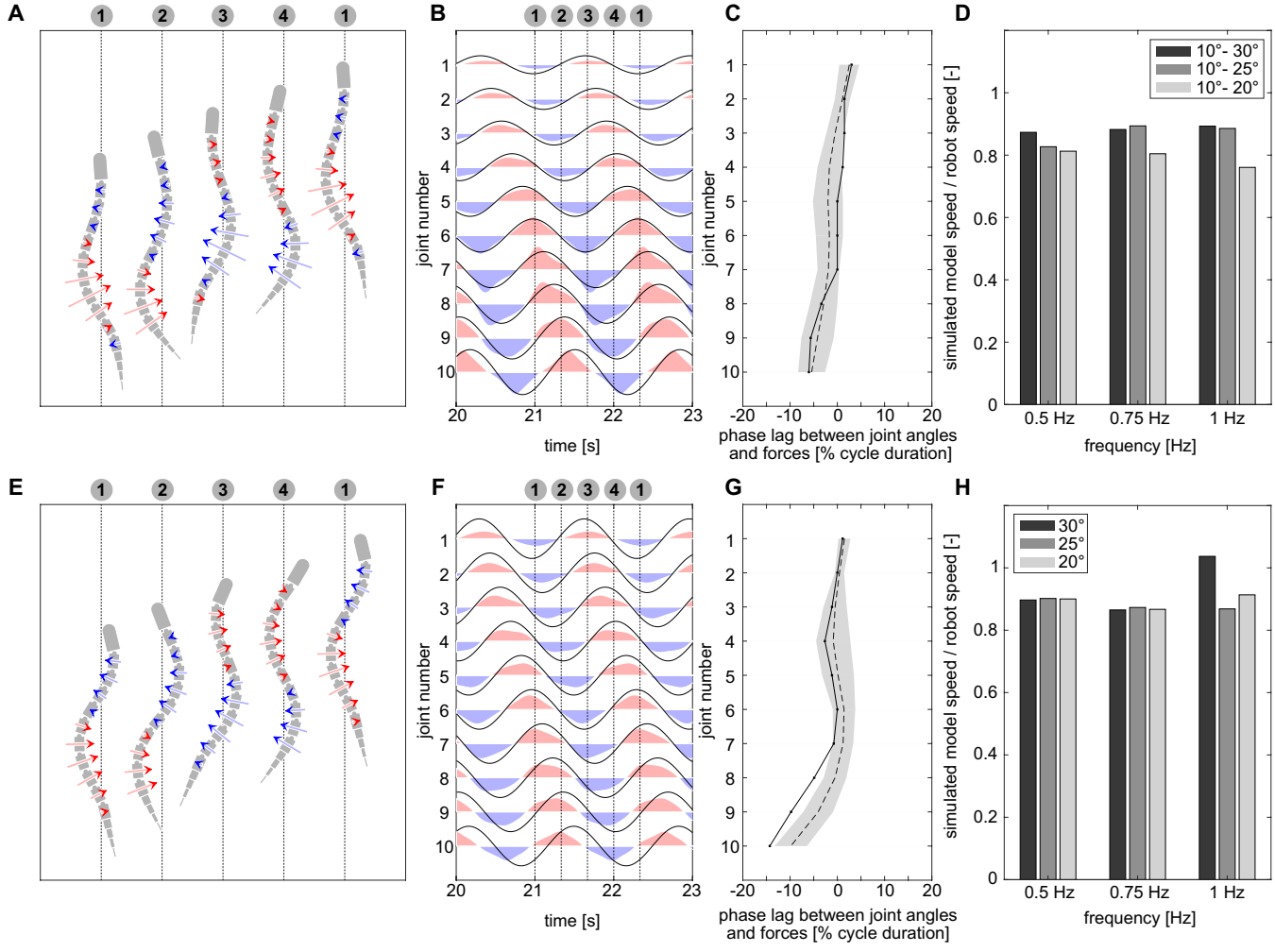

Fig. 2. Experiments to verify the relationship between timing of body bending and hydrodynamic forces during rigidly prescribed (= position control) target swimming patterns. (**A** to **C**) Position control experiments in simulation with a linearly increasing amplitude gradient from head to tail. Simulations were carried out for the gradient profiles 10° to 20° (head-tail amplitude), 10° to 25°, and 10° to 30° and for frequencies 0.5, 0.75, 1, 1.25, 1.5, 1.75, and 2 Hz. (A) Example swimming snapshots with lateral forces from the left (red arrows) and the right (blue arrows). (B) Lateral forces from the left (red) and the right (blue) over time. The solid line indicates the joint angles between segments. (C) Phase lag between joint angles and forces across all the experiments of different amplitudes and frequencies for the different segment joints. The dashed line indicates the mean; the gray shaded area indicates the SD. The solid line indicates the phase lag profile for the example shown in (A) and (B). (**D**) Validation of simulation versus robot: Comparison of ratio of forward speeds between the simulated model and the robot both in position control for different frequencies with a linearly increasing amplitude gradient from head to tail. (**E** to **G**) Respective illustrations for position control experiments in simulation with constant amplitude along the body. Simulations were carried out for amplitudes of 20°, 25°, and 30° and for frequencies of 0.5, 0.75,1, 1.25, 1.5, 1.75, and 2 Hz. (H) Validation of simulation versus robot illustrated with the ratio of forward swimming speeds in simulation and robot in position control with a constant amplitude gradient.

$$\dot{\varphi}_n = 2\pi f + \Sigma_{j=1}^{N} w_{nj} \sin(\varphi_j - \varphi_n - \psi_{nj}) + w_{fb} F_n z_n \quad (1)$$

$$z_n = \cos(\varphi_n + \chi), \chi = 0 \quad (2)$$

$$u_n = \cos(\varphi_n) \quad (3)$$

where u_n represents the local activation of the segmental circuit within a chain of $N = 10$ segmental circuits (as many as the number of actuated joints in the robot, because the local activation signals modulate the simulated muscles' activity). This local activation determines the muscle activity and hence the torque in the local joint (see the "Muscle model" section). The timing of u_n is controlled by the phase φ_n, whose time evolution is defined by three main components (the three terms of Eq. 1): (i) a local oscillator defined by its intrinsic frequency f; (ii) central coupling between segments defined by weights w_{nj} (nearest-neighbor coupling, $w_{nj} \neq 0$ for $j = n - 1$ and $j = n + 1$) and central phase lag bias ψ_{nj} that influences the number of body waves as, e.g., presented in (*49*); and (iii) the feedback mechanism based on the entrainment of the phase φ_n by the local hydrodynamic force F_n and a given feedback strength w_{fb}. F_n is the resultant normal force on a segment obtained from the difference of force readings from the left and right sensor plates. The feedback mechanism is defined by the sensitivity function z_n that characterizes how the phase information is embedded in the feedback (please find details on the choice and interpretation of χ in Supplementary Text S1 and fig. S2). Compared with similar types of models of swimming CPG circuits (*49*–*51*), the novelty here is the feedback mechanism and the study of its role in rhythm generation

and coordination in both a sensorized robot interacting with real physics and in simulation.

To determine whether hydrodynamic forces could entrain segmental activity in a more biologically realistic neural network, we also modeled the segmental circuit using a Matsuoka neural network (Materials and Methods). This network represents an elementary (central) oscillatory neural network (*52*), to which we added central coupling and the force feedback loop. The model differs most notably from the phase oscillator model by the absence of an explicit timing signal (phase) and instead indirectly establishes relative timings between signals based on the neural outputs. In such a neural network model, the force feedback mechanism is implemented by connections from the force sensors that provide excitation ipsilaterally to the segmental circuit and inhibition contralaterally (Fig. 1E). This topology is consistent with the effects of mechanosensory dorsal cell stimulation in lampreys (*20*) and with the effects of mechanosensory

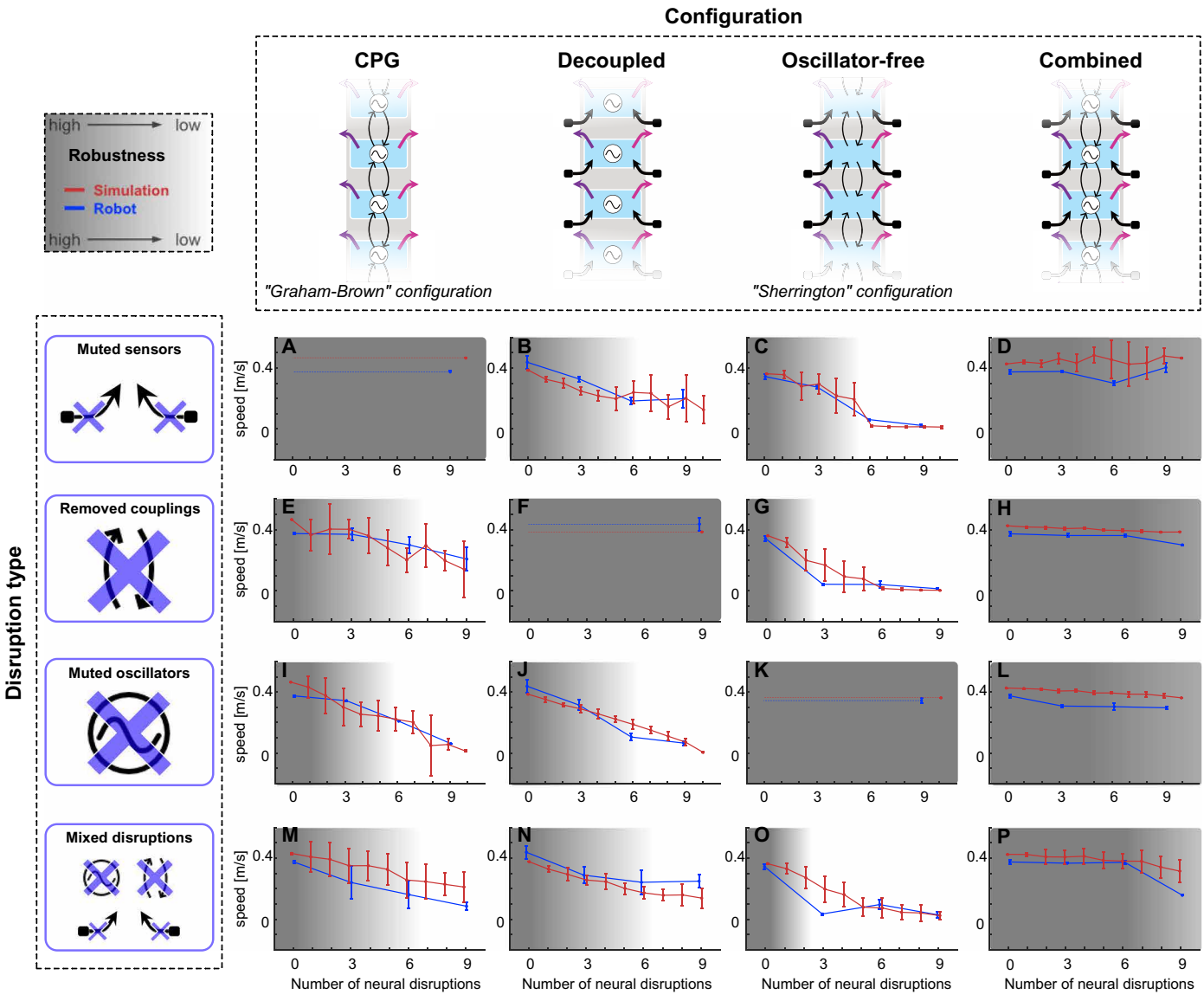

Fig. 3. Robustness to neural disruptions in segmental circuits for four model configurations. Maintaining higher swimming speed over a range of gradually increasing number of disruptions indicates higher robustness. Swimming performance is quantified by speed. (**A** to **P**) Gray gradient shading indicates the overall robustness (higher opacity = more robust) of a specific configuration exposed to a specific disruption type. Details on the implementation of the neural disruptions can be found in Materials and Methods. The decoupled and CPG configurations exhibit similar robustness performance (similar decline for muted oscillators and similar decline for mixed disruptions). The oscillator-free configuration showed lowest robustness (no swimming for more than five muted sensors and mostly lower robustness for many higher-number mixed disruptions). The combined configuration showed the highest robustness (better than CPG, decoupled, and oscillator-free configurations for mixed disruptions). Simulations (in red): Average swimming speeds of simulations are indicated in red. All data points are represented by means ± SD that reflect a series of independent randomly initialized experiments ($n = 30$ for each data point exposed to mixed disruptions and $n = 10$ for remaining disruption types). Robot (in blue): On the robot representative initial conditions of simulation runs close to the simulation mean were selected and tested. Each data point corresponds to the $n = 3$ fastest robot experiments under the same initial condition. On the robot, 0, 3, 6, and 9 simultaneous disruptions were tested. Corresponding simulation videos can be found in movie S1.

Rohon-Beard neurons that send ipsilateral excitation to the swimming circuit in zebrafish larva during the first days of life (*53*).

Control configurations and neural disruptions

Our approach provides the unique advantage of allowing the investigation of the respective roles of central and peripheral mechanisms by selectively activating and deactivating these mechanisms in simulation and in the real world when implemented in a robot. For this, we investigated four circuit configurations (Fig. 3) with different possible combinations of segmental oscillators, intersegmental coupling, and/or sensory feedback. The first configuration had only segmental oscillators and intersegmental coupling ("CPG" configuration, or "Graham-Brown configuration") but no sensory feedback. The second configuration had segmental oscillators and sensory feedback but no intersegmental coupling ("decoupled" configuration, $w_{nj} = 0$). The third configuration had sensory feedback, intersegmental coupling but no segmental oscillators ("oscillator-free" configuration, or "Sherrington configuration"). To explore this configuration with the robot, each segment was programmed to have no local oscillation ability ($f = 0$), to be explicitly coupled with its nearest neighbors ($w_{nj} \neq 0$), and to receive local hydrodynamic force feedback. The segments were all initialized with different phases to provide an initial movement stimulus to start the synchronization process. The fourth and last configuration had coupled segmental oscillators and sensory feedback ("combined" configuration). The combined configuration is likely the most representative of actual circuits in swimming animals. We used the same parameters across the four configurations, with the exception of higher feedback gains for the oscillator-free configuration.

To investigate the contribution of each circuit component in maintaining swimming speed, we introduced a set of neural disruptions that were applied to these four circuit configurations. We distinguished three types of neural disruptions, namely, muted oscillators, removed intersegmental couplings, and muted local force sensors (Fig. 3). These disruptions were applied to a gradually increasing number of targets (Materials and Methods) in the segmental circuits described in Eqs. 1 to 3. In addition to investigating the robustness to single types of neural disruption separately, we also considered a scenario with a mix of all three types of neural disruptions (Materials and Methods). Larger robustness was attributed to configurations that keep a good swimming performance despite being exposed to a gradually increasing number of these neural disruptions. In our experiments, we were interested in the propulsive characteristics of different swimming patterns, and we therefore used speed as a proxy for swimming performance (see Materials and Methods for a definition of the performance metrics).

RESULTS

Robustness of different control configurations to neural disruptions

Without any feedback, the CPG configuration (or Graham-Brown configuration) generated swimming (Fig. 3, A, E, I, and M) as in our previous studies (*49*). As expected, gradually increasing the number of neural disruptions gradually decreased swimming performance (movie S1 and see the "Neural Disruptions" section on our interactive data visualization website at https://go.epfl.ch/AgnathaX).

The decoupled configuration, which received sensory feedback, could generate swimming (Fig. 3, B, F, J, and N). This was unexpected because no intrinsic intersegmental coupling was provided by the segmental circuits, and therefore, no coordination between oscillators was centrally defined in advance. The decoupled and the CPG configurations had similar robustness to neural disruptions. When exposed to a gradual increase of muted oscillators, they showed a statistically identical decline in swimming performance [Fig. 3, I and J; Games-Howell (GH) post hoc tests $P > 0.05$ after a one-way analysis of variance (ANOVA) $P < 0.005$; all P values are reported in table S3]. In these two configurations, the decreases in speed evoked by the mixed neural disruptions were also largely identical (Fig. 3, M and N; GH post hoc test $P > 0.05$, after a one-way ANOVA $P < 0.005$, table S3).

To determine the importance of the rhythmogenic ability of the segmental circuits (i.e., the ability to generate rhythms), we removed it in the oscillator-free configuration (or Sherrington configuration). Unexpectedly, this configuration, which received sensory feedback, also generated swimming (Fig. 3, C, G, K, and O). However, it showed the lowest robustness to neural disruptions. Swimming dropped to near-zero speed for more than five muted sensors or five removed couplings (Fig. 3, C and G). Its performance was significantly lower compared with all the other configurations when four or more mixed disruptions were applied (Fig. 3, M to P; GH post hoc test $P < 0.001$ to $P < 0.05$, one-way ANOVA $P < 0.005$, table S2).

The combined configuration, which incorporated coupled segmental oscillators and sensory feedback, exhibited the highest robustness to neural disruptions both in simulation and with the robot (Fig. 3, D, H, L, and P). It performed better than the decoupled and oscillator-free configurations across all numbers of mixed neural disruptions (Fig. 3, N to P; GH post hoc test $P < 0.001$ to $P < 0.05$, one-way ANOVA $P < 0.005$, table S2) and better than the CPG configuration when six or more mixed neural disruptions were applied (Fig. 3, M and P; GH post hoc test $P < 0.001$ to $P < 0.05$, one-way ANOVA $P < 0.005$, table S2).

We also quantified the time needed to reach steady-state swimming patterns by measuring the time to converge to the final overall phase lag along the body. The CPG configuration exhibited the fastest convergence to the steady state among all the configurations as shown by a separate analysis of transient times (fig. S3). The configurations that included sensory feedback had longer transient times due to the additional disturbance caused by the sensor signals. Nonetheless, the combined configuration showed shorter transients than the other configurations that included sensory feedback (decoupled and oscillator-free configurations). This illustrates another benefit when central mechanisms are combined with peripheral mechanisms.

Decoupled configuration reveals intersegmental entrainment mechanism

Next, we examined the source of swimming robustness in the decoupled configuration where a major component of the CPG (i.e., intersegmental coupling) was absent (Fig. 4A). The robot experiments revealed that intersegmental phase lags $\Delta\varphi_i = \varphi_i - \varphi_{i+1}$ converged to strictly positive values (Fig. 5 and Materials and Methods) and thus induced a self-organized traveling wave of undulations from head to tail (overall phase lag with mean ± SD: 78.70 ± 5.95%, $n = 6$; Fig. 4A and movie S2). We extended the analysis with simulations and found that traveling waves occurred over a range of oscillator intrinsic frequencies and sensory feedback strengths (fig. S4 and movie S3). This result indicates that the

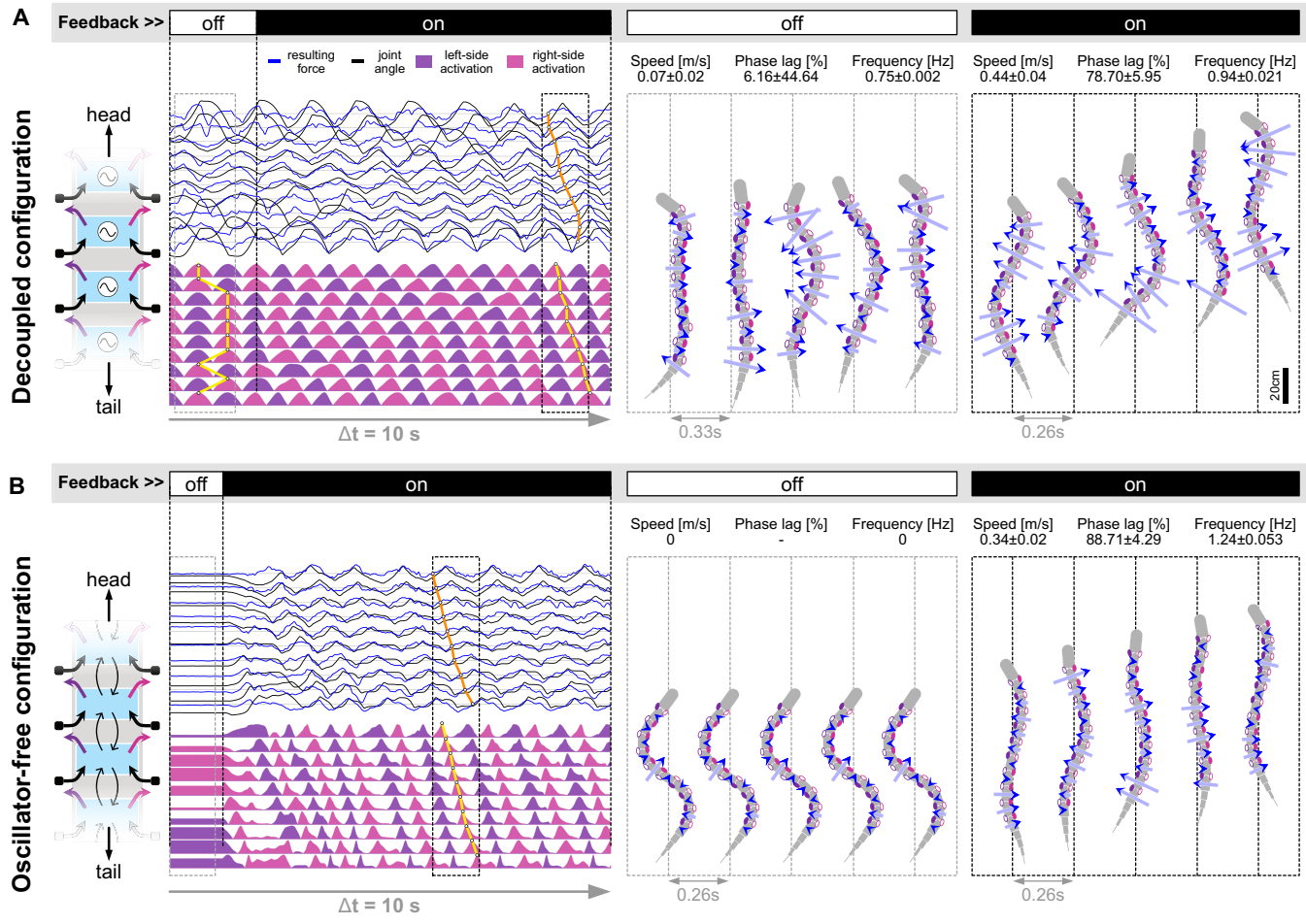

Fig. 4. Sensory feedback for undulatory swimming provides redundancy to central mechanisms in intersegmental coordination and rhythmogenesis. (**A**) Representative example of a robot experiment under the decoupled configuration, starting from random initial conditions and sensory feedback turned off. Once the feedback is turned on, intersegmental coordination is established, and a traveling wave emerges. Mean ± SD values for speed, overall phase lag, and frequency are shown for $n = 6$ robot experiments with an intrinsic oscillator frequency of 0.75 Hz and randomly initialized phase oscillators. (**B**) Representative example of a robot experiment under the oscillator-free configuration, starting from random initial conditions and sensory feedback turned off. With sensory feedback turned on, spontaneous rhythmogenesis emerges and results in a traveling wave along the body. Mean ± SD values for speed, overall phase lag, and frequency are shown for $n = 11$ robot experiments with a central overall phase lag bias of 100% (cycle duration) and randomly initialized phases in the segmental circuits. Example videos of the swimming robot for both configurations (A and B) are provided in movie S2.

hydrodynamic force feedback can serve as an intersegmental entrainment mechanism in the decoupled configuration. Higher feedback strengths resulted in higher frequencies and larger overall phase lags along the body (fig. S4).

The positive phase lag emerged because of two key asymmetries in the neuromechanical model: a structural body asymmetry and a spatial shift between actuation and perception (Supplementary Text S2, fig. S5, and movie S4). Each of these asymmetries was sufficient to generate positive phase lags. Pressure-sensitive dorsal cells in the lamprey tend to have receptive fields that are caudal to their position in the spinal cord (*18*, *19*), suggesting that they also have such spatial shifts between actuation and perception. Using a theoretical analysis (Supplementary Text S3), we found that the force feedback produces short- and long-range interactions between the local oscillators, because the phase states of the oscillators are embedded in the local force measurements. This results in a complex network of oscillators, coupled by the mechanical and hydrodynamic interactions between each segment. Synchronization and positive phase lags are emerging (self-organizing) properties of this complex network shaped by the physics of locomotion.

Oscillator-free configuration can generate spontaneous oscillations

Similarly, we next examined the source of swimming robustness in the oscillator-free configuration, where the other main component of the CPG (segmental rhythmogenesis) was absent. Our results with this configuration show that the local hydrodynamic feedback could generate spontaneous oscillations without the need for intrinsic oscillatory centers. Similar to the decoupled configuration, we found nonzero forward speeds when no neural disruption was applied in simulation, with speeds close to the other configurations (Fig. 3). Robot experiments showed that oscillations emerged and resulted in forward swimming (Fig. 4B and movie S2). Additional simulations (fig. S6 and movie S3) revealed that spontaneous

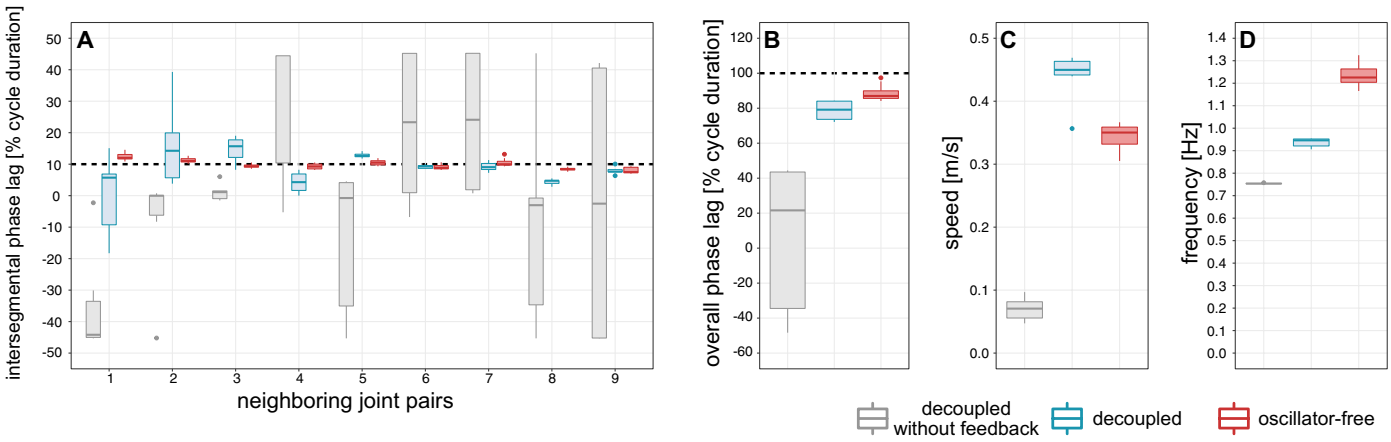

Fig. 5. Performance results of robot experiments in the decoupled and oscillator-free configurations. The decoupled configuration with and without feedback were each tested in $n = 6$ experiments at an intrinsic frequency of 0.75 Hz. The oscillator-free configuration was tested in $n = 11$ experiments and a central phase lag bias of 100% (cycle duration). The oscillator phases were randomly initialized in all experiments. The performance metrics in (**A**) to (**D**) are described in Materials and Methods. The horizontal lines indicate the median. Box limits are the upper, and lower quartiles and the whiskers show the values within a 1.5 x interquartile distance from the upper and lower quartiles, respectively. Outliers are represented as dots. Note that in (A), the intersegmental phase lag at the first joint for the decoupled configuration is not strictly positive. The dynamics of this joint would need more time to converge; however, we were limited by the size of the swimming pool.

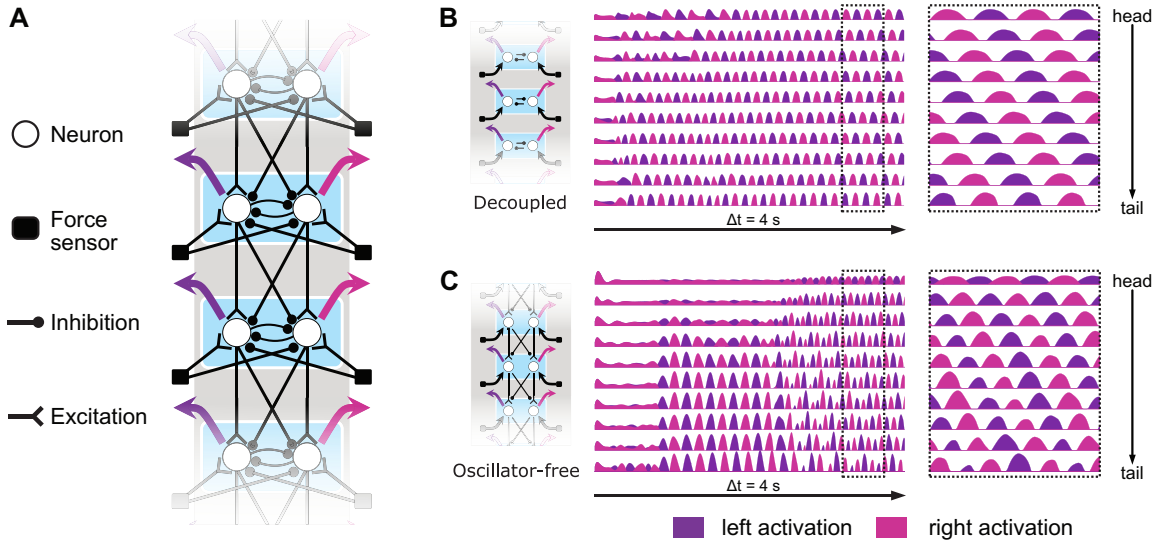

Fig. 6. Neural network implementation of the segmental circuits. (**A**) Excitatory and inhibitory connections in the computer-simulated Matsuoka neural network model. (**B**) Example simulation of the decoupled configuration showing the emergence of a traveling wave in the output of the neuron of the left and right sides that is sent as activation to the muscles. (**C**) Example simulation of the oscillator-free configuration showing the emergence of a traveling wave in the neuron outputs.

swimming rhythms emerged for (i) sufficiently high sensory feedback strengths (fig. S6B) and (ii) overall central phase lags between 100 and 140% of the cycle duration (fig. S6D). These simulations also showed a positive correlation between feedback strength and overall emerged phase lag (positive phase lag values between 49.6 and 92.7%; fig. S6B) similar to the decoupled configuration, however, spanning a wider range of overall phase lags (oscillator-free, 73.29 ± 19.69% cycle duration; decoupled, 104.23 ± 14.08% cycle duration, means ± SD).

Both the decoupled and the oscillator-free configurations represent key examples that illustrate how the feedback entrainment mechanism contributes to the establishment of swimming patterns. This can be seen as a self-organized process involving interactions between the feedback mechanism, the body, and the environment.

Entrainment in a phase-free neural network model

In addition, to the phase oscillator model, we tested these two specific configurations with the more biologically realistic network that controlled the simulated body (Fig. 6A). The decoupled configuration was implemented by removing intersegmental coupling ($\eta_{2,c} = \eta_{2,i} = 0$), whereas the oscillator-free configuration was explored by removing the mutual inhibition within segments ($\eta_1 = 0$). In both configurations, we found traveling waves of body undulations emerging (Fig. 6, B and C), thus showing that the proposed feedback

mechanism can successfully entrain neural activation while not requiring the notion of an explicit phase. In other words, the neural couplings from the force-sensing neurons (with excitatory ipsilateral projections and inhibitory contralateral projections) have an effect in this neural network that is equivalent to the sensitivity function in the phase oscillator implementation.

DISCUSSION

We found that intersegmental coordination and oscillations underlying undulatory swimming can be generated by either the CPG or sensory feedback, and this redundancy contributes to the increased robustness of swimming against neural disruptions. The neural circuitry controlling locomotion in vertebrates comprises three main components: (i) the spinal segmental circuits (part of the central nervous system), (ii) sensory inputs to the segmental circuits (peripheral nervous system), and (iii) the descending systems (central nervous system) that send commands and receive ascending inputs from the segmental circuits (*54*, *55*). A major challenge in neuroscience is to decipher the respective role of these components on the generation of locomotor movements. Here, we explored a reduced system comprising a single type of sensory input (exteroceptive feedback) and the spinal segmental circuit, both interacting with hydrodynamic forces through a robot equipped with force sensors in simulation or in the real world. The topology of the exteroceptive feedback that we used is consistent with the effects of dorsal cells in lamprey, which increase motor output ipsilaterally and decrease it contralaterally (*20*). It is also consistent with that of mechanosensory Rohon-Beard neurons that excite ipsilateral spinal rhythmogenic neurons during the first days of life of the zebrafish larva (*53*). The slowdown observed when disrupting Rohon-Beard neurons in zebrafish larva [(*14*); for review, (*15*)] is consistent with our results, despite a difference between larval fishes swimming at low Reynolds numbers and our robot swimming at higher Reynolds numbers (*53*).

One limit of our approach is that we only explored exteroceptive sensory inputs. However, we expect that proprioceptive inputs constitute another redundant source of feedback to the swimming CPG. Proprioceptive feedback is provided in lampreys by stretch sensors called edge cells that detect spinal cord stretching and that participate in motor burst termination by exciting ipsilateral segmental neurons and inhibiting the contralateral ones (*12*–*14*, *17*, *56*–*58*). The connectivity of lamprey edge cells onto the segmental circuitry is similar to the one used here for exteroceptive feedback [(*12*–*14*, *17*, *56*); for review, (*59*)]. In zebrafish, proprioceptive feedback is provided by Kolmer-Agdhur cells that detect the local movements of the cerebrospinal fluid in the central canal of the spinal cord and that send inhibitory input to the ipsilateral segmental motor circuits, and their silencing slows down swimming (*60*, *61*). Such slowdown is coherent with a certain level of redundancy between exteroceptive and proprioceptive feedback as we propose here. However, we are aware that these feedbacks are not equivalent. We also omitted the corollary discharge ascending from the spinal cord, which influences the activity of reticulospinal cells that carry the locomotor command to the spinal CPG in lamprey and in other vertebrates (*62*, *63*). We expect an increased stability of motor patterns when all of the partially redundant mechanisms of stretch- and pressure-sensitive feedback loops and the reticulospinal system work together to generate and maintain swimming, in line with previous simulation results (*54*) and neurophysiological results (*64*). Future studies could make use of our unique robot platform to test additional motor control hypotheses that are difficult to study in intact animals, e.g., to determine how descending commands interact with the effects of sensory feedback when the animal needs to adapt its locomotor movements to a turbulent flow or different fluid viscosities or to perform steering movements when, e.g., tracking a target.

An important result is that the CPG and sensory feedback play redundant roles in the generation of locomotor movements. Although our study is limited to swimming, this phenomenon could contribute to explain why it is sometimes difficult in vertebrate animal models to identify a single population of spinal interneurons responsible for locomotor rhythmogenesis, which furthermore relies on different rhythmogenic populations recruited as a function of speed as, e.g., in zebrafish (*65*, *66*) or mouse [for review, (*4*, *9*)].

Our findings also suggest that exteroceptive sensory feedback plays a notable role in the recovery of locomotor movements after full spinal transection, i.e., when the spinal CPG does not receive the descending drive from the brain and does not send ascending information to the brain anymore. Exteroceptive mechanoreceptors could favor sensory-based coupling across a disconnection in the nervous system and thus contribute to the coordination of swimming lampreys after spinal transection. Such a role may be different from one species to another. Eels can swim despite full transections in one or even two places of the spinal cord, with muscle activity that remains oscillating and frequency-locked with the segments above the transections (*10*). Lampreys can swim after a full spinal transection behind the gills (*7*). In contrast, salamanders swim only after partial regrowth of the descending fibers originating from reticulospinal neurons and spinal neurons above the lesion (*67*). In mammals, it is well established that limb sensory feedback below the lesion plays a role in the reestablishment of rhythmic locomotor activity below the lesion [(*68*–*70*); for review, (*71*)]. Our study confirms that there are important functions provided by peripheral mechanisms that might be "hidden" by well-known central mechanisms and that could play an important role in recovery of motor function after spinal cord injury.

Another important result is that the body properties dictated the perceived hydrodynamic forces, and this resulted here in a net tendency to generate forward swimming. Well-timed interactions between a passive body and local vortices are sufficient to make a dead trout body swim forward under specific conditions ["Karman gait" (*72*, *73*)]. The viscoelastic properties of the body interacting with the water therefore play an important role in self-organized swimming and in the redundancy of information carried by the sensory feedback systems discussed above. The body is also important to provide the asymmetry needed for the emergence of forward swimming (as opposed to swimming in place or backward). Our work shows that the structural asymmetry of the body (i.e., a head element that is larger than the other body segments, and the passive flexible tail at the end of the body) was sufficient to generate positive phase lags (Supplementary Text S2, fig. S5, and movie S4). In addition, a spatial shift between actuation and perception also helped favoring forward swimming.

Together, we identified the benefits of peripheral locomotion control in concert with central control and demonstrated the redundant mechanisms for rhythmogenesis and intersegmental coordination that provide explanations for the remarkable robustness of the locomotor system in undulatory swimmers. These results

further provide solutions for robust undulatory swimming robots and have implications for the design of modular robotics with distributed control (*74*–*77*). At the core of our approach lies a robot that allowed us to investigate hydrodynamic force feedback loops and to test them in a physical system interacting with the surrounding water. The presented robotic system equipped with a decoupled control scheme invokes self-organized swimming. As a result, such a system exhibits scalable characteristics that support easy construction and deployment of larger or many swimming units with a high degree of reconfigurability and robustness, e.g., for search and rescue missions or environmental monitoring (*32*, *78*, *79*) or conceptually for micro- and nanorobots for biomedical purposes (*80*). In addition, the modular design of the robot with its redundant components for pattern generation based on central and/or peripheral control provides a mechanism for high fault tolerance (*81*, *82*). The robot is remarkably resilient to both communication failures between segments and sensor failures because intersegmental coordination is provided by redundant mechanisms (note that for practical reasons, these failures are here simulated in software as opposed to actually applied to hardware). This is an important feature for applications that require robots that operate robustly in difficult environments (e.g., pipes, flooded caves, and frozen lakes) where human retrievals or repairs are not possible.

In our study, we presented a subset of the functionalities that are desirable for missions in the field, namely, robustness with regard to fault tolerance. Other behaviors like steering or backward swimming are crucial for such applications and can be implemented on top of our local control scheme. Backward swimming can be obtained by introducing an alternative force feedback scheme (see Supplementary Text S2 and fig. S5A), by changing the phase bias of the intersegmental coupling (changing the sign of ψ_{nj}), or by respectively decreasing and increasing the intrinsic frequencies of the first and last segmental circuits, similarly to what is hypothesized to happen in the lamprey (*83*). Steering can be achieved in different ways, most easily by centrally inducing a bias in the left/right muscle activation (*84*). On the basis of these elementary components for navigation, goal-oriented swimming can then be implemented on top of our control structure using existing approaches and including additional sensory cues (*32*, *85*, *86*). Field missions also require swimming with resilience to external perturbations. Here, further analyses of the controller performance under such conditions are needed in future work, and previous studies can help to increase this robustness (*87*).

Last, this robot provides the opportunity to solve engineering problems related to the stability of underwater vehicles in unsteady flows (*44*). Whereas previous robots equipped with artificial lateral line or pressure sensing systems were able to detect and respond to certain types of flow accelerations (*45*, *88*, *89*), our robot with its segmented body and the distributed sensing and actuation provides a potentially finer scale of control along the entirety of the body to respond to flow perturbations and paves the way for future studies on advanced maneuvers in unsteady flows.

MATERIALS AND METHODS

Robot design

We designed and implemented the undulatory swimming robot called AgnathaX (inspired by the Agnatha superclass of jawless fish that includes lamprey, and X = number of 10 robot segments) for the purpose of this study. AgnathaX is a modular lamprey-like robot built out of 10 active body modules that feature easy integration with exteroceptive sensors, a head unit for computations, and a passive tail. AgnathaX weighs 4.2 kg and spans 1250 mm in length (fig. S1A). This waterproofed robot is controlled wirelessly and can move with both position and torque commands at the surface of the water. Each of the 10 body modules (90 mm in length and 0.35 kg of mass) is actuated by a Dynamixel MX-64AR servomotor (Robotis) that is attached with custom aluminum frames. The standard Dynamixel protocol (RS-485 bus at 1 Mbps and 4P cables) was used to communicate to the servomotors. A safety limit of ±60° was programmed for each servomotor to prevent self-collisions. The head unit of the robot contains an Odroid XU4 (Hardkernel) computer running Linux. The computer acquires the external sensor signals from all body modules as well as the full state of the motors (i.e., position, speed, voltage, and current) and evaluates the distributed controllers for each module in a 100-Hz control loop. The corresponding output commands of each controller are sent back to the motors to move the robot. Data gathered from the sensors and motors and the states of the controllers were logged during swimming experiments and were used for posterior analysis. The robot has three independent lithium polymer batteries. One battery is placed on the tail module (nominal voltage of 11.1 V and capacity of 1500 mAh) and powers the motors. The remaining two batteries are located on the sides of the head unit, keeping the center of mass aligned with the centerline of the robot. The first battery at the head powers the external sensor array (7.4 V and 800 mAh), and the second battery powers the computer (11.1 V and 1500 mAh) through a 5-V DC/DC regulator (25-W). The maximum operating time of the robot is 30 min, given by the fastest decaying battery for the motors. All batteries have a nominal discharge rate of 25°C. The tail was designed using two flexible polyethylene terephthalate sheets of 1-mm thickness. The shape (resembling a real lamprey tail), material, and thickness of the tail were designed to ensure that the tail resonates (i.e., achieves larger lateral bending) at nominal robot undulation angles of ±30° and a frequency of 0.75 Hz. This choice of design parameters resulted from experiments with a number of materials and shapes that were carried out similarly by Leftwich *et al.* (*40*). A protective soft, hydrophobic, and highly flexible wrapping sleeve was used to cover the robot modules (i.e., head, body, and tail) before it was put into a custom waterproof swim suit. The suit was fabricated with a yellow ripstop fabric coated with a thermo-adhesive material. The seams of the suit were sealed using heat and high pressure (heat press), where the thermo-adhesive material glued the parts together in the process. A zipper (TIZIP, MasterSeal 10, 500-mbar pressure proof) at the head of the robot was used to allow access to the robot modules. In addition, the head unit connects to the external sensors through the suit by means of a plug (Binder, 7-pole, 693 series), guaranteeing IP67 waterproofing.

Hydrodynamic force sensing on the robot was implemented by means of force plates that are capable of measuring the normal forces acting on either side of each segment. Each force plate module consists of an aluminum frame that attaches to the corresponding frame of the robot segment inside the waterproof suit by means of an array of magnets. The magnets lock both frames in place and prevent them from detaching or changing orientation as the swim suit is deformed according to the actuated robot modules. Each force plate module has two load cells of 300gf TAL221 (Shaanxi HT Sensor Technology) and two carbon fiber plates of 60 mm by 44 mm with a thickness of 2 mm. The carbon fiber plates were designed to

remain parallel to the robot body and thus sense normal forces. Each load cell was connected to an amplifier HX711 (Sparkfun), and their amplified signals were sent to an Arduino Mini board (Arduino). A custom-printed circuit board attached to the Arduino was designed, which integrates a 5-V voltage regulator to power the Arduino and the load cell amplifiers. All the electronic parts (i.e., amplifiers and Arduino board) were sealed and waterproofed using Sicomin GreenPoxy 56 (Swiss-Composite). The Arduino boards were connected, and a custom serial data protocol was used for communication. Noise on the sensors originates from the small amplifier's excitatory high-frequency voltage ripples and from perturbations by small waves stemming from reflections of the pool walls. Therefore, a median filter was applied before passing them to the feedback control. Note that the forces measured by these custom-designed sensing units are the result of complex flow patterns surrounding the robot that include both parallel and perpendicular components with respect to the sensing plates and also include vortices. All these flow structures contribute to a pressure field that consequently determines the interaction forces of which we measured the normal component using our sensors. Note that because the plates are surrounded by water on both sides, the sensors do not measure hydrostatic depth-dependent pressure. Each of the force plates can sense pushing and pulling forces. In our present study, we focused on the resultant normal force, which is determined by the difference of the two lateral force plate measurements. The range of the resulting normal forces at a segment was about ±0.3 N for fast swimming gaits of 0.4 m/s. We were able to obtain a sensing resolution of 0.004 N with our force sensor units.

Last, we found that the addition of the external sensor units led to a shift of the center of mass. To ensure that the center of buoyancy lies above the center of mass centerline (reduces rolling during swimming), an array of low-density foam floats (60-mm diameter and 30-mm thickness) were added on top of the suit. These floats were fixed in position by a magnet that attaches to a magnet on the top of each motor segment. These floats housed a light-emitting diode (LED) that was connected to their respective Arduino sensor board and was used for motion tracking. In addition, one LED at the head and three LEDs at the tail were used to track the robot during the swimming experiments.

Robot experiments

The experiments were carried out in an indoor swimming pool of 2 m by 6 m and a depth of 31 cm. A dual-camera tracking system (Basler A622F) mounted 2.25 m above the pool surface was used to track the position of the LEDs at a sampling rate of 15 Hz and calibrated for an accuracy of less than 1 cm. Low ambient light was used during the experiments to increase the contrast with the background for reliable LED tracking. An additional Hero 4 session camera (GoPro) was placed on top of the pool to record the robot movements. Initial position and orientation of the robot at each experimental run was set manually. This prevented the robot from quickly deviating and touching the side walls of the pool. We considered experiments successful when the robot was swimming at least three-quarters of the swimming pool before colliding with the walls or doing a hard stop.

Muscle model

Viscoelastic body deformations are introduced between segments by a muscle model derived from an antagonist muscle pair (*90*), approximated as linear spring dampers, and adapted for rotational joints

$$\tau_n = \alpha u_n - \gamma \theta_n - \delta \dot{\theta}_n \quad (4)$$

It generates a torque τ_n in the nth joint of the segmented body and contains the muscle activation u_n, the activation gain α, the stiffness γ, and the damping δ. The activation signal u_n is produced by the segmental circuit (Eq. 3). It controls the internal torque and serves therefore as a way to induce bending to either side of the body (contracting on the right when $u_n > 0$ and on the left when $u_n < 0$). At the same time, a counteracting torque is generated depending on the kinematic state of bending angles (θ_n) relating to stiffness and angular speeds ($\dot{\theta}_n$) relating to damping. This model assumes a fixed left-right intrasegmental coordination, in which the muscle pair operates in antiphase. The muscle model in Ekeberg's original contribution (*90*) contained an additional actively controlled stiffness term (cocontraction of muscles), which we omitted here.

To find suitable muscle parameters for the real-world robot model, we used a response surface method (*91*) to systematically find the muscle parameters that maximize the forward speed of the robot. For this purpose, the CPG configuration was used with an overall central phase lag bias of 100%. We designed an experiment that consisted of $n = 20$ test runs following a central composite design matrix with parameter ranges [0.1, 1], [0, 2], and [−0.05, 0.05]. A generalized second-order polynomial function (including interaction terms) was fitted using the resulting forward speeds. The resulting model showed that high speeds were obtained at values close to $\alpha = 1$, $\gamma > 1$, and δ close to zero. Therefore, we selected the parameters $\alpha = 0.9$, $\gamma = 1.6$, and $\delta = 0$ (the corresponding simulation parameters are slightly different and can be found in table S1). Larger values of α led to higher bending amplitudes and often saturated at the maximum bending angles of the motors. The stiffness γ had a strong effect on the swimming trajectories of the robot. A value of $\gamma = 1.6$ provided straighter trajectories for oscillator-free and combined configurations, whereas $\gamma = 1.2$ provided better trajectories for the decoupled configuration. Despite the fact that we used two different values of γ, the resulting speed was similar for values within that range according to our model fitting results. Although we set the damping parameter in the robot experiments to zero, mechanical damping was still present in the joints of the robot because of dissipative effects in the motor mechanics.

Simulated rigid body model

The elongated swimming body was modeled in Webots 6.4.4 (Cyberbotics), a simulator based on the Open Dynamics Engine. The segmented elongated swimming body was constructed from a head segment, 10 identical body segments, and a segmented tail. The segments were linked with two-dimensional hinge joints that restricted the movements of the swimmer within a plane. The tail joints had spring-damper properties and were used passively, whereas the segmented body was actuated by torques in the joints between body segments produced by the simulated pairs of muscles. Corresponding dimensions, weights, stiffness, and damping for the body and the tail are given in fig. S1B and table S1.

Simulated hydrodynamics

We simulated the hydrodynamic environment for our anguilliform swimmer using the model proposed by Porez *et al.* (*47*). This model

provides the external forces acting on the simulated rigid body model on the basis of its kinematic state. It is based on Lighthill's large amplitude model (*92*) and considers reactive forces stemming from the acceleration of the fluid moved by the swimming body, as well as resistive (drag) forces from viscous stresses in the boundary layer of the body. Furthermore, this model allows for numerical integration close to real time due to a Newton-Euler modeling approach, which greatly decreases simulation time for different sets of parameters. We evaluated the physics (swimming model including the hydrodynamics) at 0.5-ms time steps. In comparison, the controller, which sets the corresponding muscle activations and torques, was running at a time step of 5 ms. We validated this model against the AgnathaX robot (Fig. 2, D and H).

In addition to reactive and resistive forces, buoyancy was modeled following Archimedes' principle, which states that the buoyant force for a given body corresponds to the weight force of the fluid that it displaces and acts at the centroid of the displaced volume. We computed the immersed volume and the centroid for each segment with the following steps. First, the intersections between the edges of the parallelepiped and the water surface were calculated (the force was only computed for the parallelepiped in each module; the final value was multiplied by a constant factor to compensate for the additional cylindrical volume). Then, the intersection points were ordered using a Gift wrapping algorithm to form the top surface of the immersed polyhedron. The volume and the centroid of the immersed polyhedron were calculated using Mirtich's formulas (*93*). Our swimming body is positively buoyant and swims at the surface of the water.

Neural network model

This model is based on excitatory and inhibitory connections between neurons (Fig. 6A) and illustrates how the segmental circuit interacts with the local force sensors by means of these connections. We defined our neural network as follows:

$$\dot{x}_{n,i} = \frac{1}{\tau}(-x_{n,i} - \beta \nu_{n,i} + \eta_1 [x_{n,c}]^+ + \eta_{2,c} [x_{n-1,c}]^+ + q) + b_i F_{n,i} + b_c F_{n,c} \quad (5)$$

$$\dot{\nu}_{n,i} = \frac{1}{\alpha\tau}(-\nu_{n,i} + [x_{n,i}]^+) \quad (6)$$

$$y_{n,i} = [x_{n,i}]^+ \quad (7)$$

In this "Matsuoka" (*52*, *94*) neural network model, the two states x and ν describe the membrane potential and the self-inhibitory input (fatigue or adaptation) for a neuron, respectively. The corresponding output $y_{n,i}$ of each neuron is non-negative and defined as $[x]^+ = \max(0, x)$. The indices i and c indicate the location of the neurons on the respective ipsilateral and contralateral side; n denotes the segment number starting from the head. τ represents the time constant of the neuron and relates to oscillation frequencies (α and β are constant gains). Connectivity between neurons is defined by intrasegmental influence η_1 and intersegmental influence $\eta_{2,c}$ and $\eta_{2,i}$, thus defining the central coupling in the control system. In addition, each neuron receives an excitatory tonic input q that induces spontaneous firing. The output of each neuron directly provides the activation of the virtual muscle on the respective side ($u_n = y_{n,i} - y_{n,c}$) and contributes to body deformation.

The feedback mechanism relies on the lateral pressure-based forces $F_{n,i}$ and $F_{n,c}$, where the respective ipsilateral neurons get excited when forces acting from the water toward the body on the same side are sensed and inhibited when forces acting from the water toward the body are sensed on the contralateral side. As a result, neuron activities are synchronized with the external forces following the same general entrainment principle as for the phase oscillator model. This feedback topology is very similar to the connectivity of stretch-sensitive edge cells in lampreys (*14*). The corresponding connectivities are illustrated in Fig. 6A.

Parameter tuning and network design

The coupling weights w_{nj} in our phase oscillator model were hand-tuned to obtain a quickly converging and steady-state swimming pattern in the CPG configuration. This was required to not interfere with the additional transient behavior that is caused by the feedback mechanism. The central phase lag bias ψ_{nj} was chosen to impose an overall phase lag of 100% along the body because this leads to fast undulatory swimming. Our goal with the Matsuoka neural network model was to show that the feedback mechanism produces the same swimming patterns in a control system without the notion of an explicit timing signal (phase). Therefore, the neural network model was designed in a bottom-up approach. We started with the oscillator building blocks that rely on mutual inhibition and the feedback connections with ipsilateral excitatory and contralateral inhibitory connections. In a next step, minimal coupling was introduced by excitatory downward connections. Additional contralateral inhibitory coupling connections were lastly added for increased stability of the system. Parameters were then tuned similarly to the phase oscillator model, starting with the intrasegmental connections, followed by intersegmental couplings, and lastly feedback strength. All the segmental connections were tuned by incrementally increasing their strength until the "CPG configuration" would quickly converge to again minimize the interference with transient behavior from the feedback.

For both models (phase oscillator model and neural network model), we tuned the feedback gains by incrementally increasing their values to obtain entrainment and forward swimming for the decoupled and oscillator-free configurations. We used the same parameters for all four configurations, with the exception of higher feedback gains for the oscillator-free configuration. Parameter values are listed in table S1. Our parameter tuning procedure provides good swimming performance; however, there is potential for further optimization using, e.g., learning-based methods.

Implementation of neural disruptions

We considered three types of neural disruptions in our experiments (on the real robot and in simulation): muted oscillators, removed intersegmental couplings, and muted local sensors. Muted oscillators were implemented by setting the corresponding intrinsic frequencies of oscillators to zero ($f = 0$). The intersegmental couplings were removed by setting the respective coupling weights to zero ($w_{nj} = 0$). At last, we muted the local sensors by setting the respective feedback strength to zero ($w_{fb} = 0$).

These three different neural disruption types were first evaluated in a series of simulations (allowing us to carry out a large number of experiments) that we divided into four scenarios. The first three scenarios incorporated each neural disruption type separately. The first scenario had only muted oscillators, the second scenario had

only removed intersegmental couplings, and the third scenario had only muted local sensors. In each of these scenarios, we applied neural disruptions at random locations in the simulated spinal network while we progressively increased the number of neural disruptions starting from one in increments of 1 up to 9 (for the removed couplings) or 10 (for the muted oscillators and local sensors). In addition, we repeated simulations $n = 10$ times for a given number of neural disruptions, where each simulation was carried out for a different set of random neural disruption locations. Using this procedure, we were able to capture the variability in forward swimming performances depending on the frequency of the neural disruptions. Last, in the last scenario, we used a combination of the three neural disruption types (mixed disruptions). Analogous to the three preceding scenarios, we applied neural disruptions at random locations while progressively increasing the number of disruptions from one in increments of one up to nine. However, each disruption in this scenario could be one of the three possible neural disruption types at a random location (see Supplementary Text S4 for an example). This procedure was then applied for a progressively increasing number of neural disruptions, where, again, for a given number of disruptions, the simulations were repeated ($n = 30$) as for the three previous scenarios. More simulations for a given number of neural disruptions were carried out to account for the increased variability due to the different neural disruption types compared with the first three scenarios with single neural disruption types only.

In the last step, we complemented the simulation study with corresponding robot experiments to confirm our findings in real-world physics. For this purpose, we picked specific neural disruption settings closest to the average behavior in simulation at the data points of 0, 3, 6, and 9 neural disruptions for all the different configurations and neural disruption types (Fig. 3). Each of these specific neural disruption settings was then repeated up to five times, and the fastest three swimming experiments were considered for the analysis.

Performance metrics

Frequency

We used the autocorrelation function to determine the frequency of swimming gaits, because the shape of the considered signals (joint angles) can vary in shape because of adaptations by the feedback loops, making it more robust than measuring the time difference between zero-crossings. The autocorrelation function measures the correlation between a given signal and its time-delayed copies. Highest correlation values indicate periodic delays (cycle duration), which can be used to compute the frequency as the inverse of the cycle duration. We used MATLAB's autocorrelation function from the Econometrics Toolbox

$$f = \frac{1}{T} = \frac{1}{N}\sum_{i=1}^{N}\frac{1}{T_i} \tag{8}$$

$$T_i = \text{autocorr}(\theta_i(t)) \tag{9}$$

where N describes the number of joints, f describes the frequency, T describes the period averaged over all the joints, T_i describes the estimated cycle duration for joint i, and θ_i describes the ith joint angle.

Speed

The speed for a particular swimming run is computed over the two last cycles of the experiment, where the cycle time is computed from the frequency (see above). The speed $\hat{v}$ is computed as the average over all the instantaneous speeds $v(t)$ occurring in the two-cycle period. The corresponding instantaneous speed is computed from the head displacement between the current time instance and a cycle period ago, taking into account the direction of movement $\overrightarrow{dx}$ (forward or backward)

$$v(t) = \text{sign}(\overrightarrow{dx})\frac{|\vec{x}_{\text{head}}(t) - \vec{x}_{\text{head}}(t-T)|}{T} \tag{10}$$

$$\hat{v} = \frac{1}{2T}\int_{t_{\text{end}}-2T}^{t_{\text{end}}} v(t)\,dt \tag{11}$$

This performance metric is robust to turning patterns because if a slightly turning swimmer and a swimmer that follows a straight line achieve the same speed, then their performance is considered equal.

Intersegmental and overall phase lag

Analogous to the frequency computation, we used the cross-correlation function to determine the instantaneous intersegmental phase lag $\Delta\varphi_i(t)$ of signals between consecutive joints. We used MATLAB's cross-correlation function from the Econometrics Toolbox. Each instantaneous intersegmental phase lag at time t was computed over a fixed time window $[t - t_W, t]$. To compare gaits of different frequencies, the intersegmental phase lags were normalized by the corresponding cycle durations. We defined the instantaneous overall phase lag $\Delta\Phi(t)$ as the sum of intersegmental phase lags

$$\Delta\Phi(t) = \sum_{i=1}^{N}\Delta\varphi_i(t) \tag{12}$$

$$\Delta\varphi_i(t) = \frac{\text{crosscor}(\varphi_i^{[t-t_W,t]}, \varphi_{i+1}^{[t-t_W,t]})}{T} \tag{13}$$

Subsequently, we defined the steady-state intersegmental and overall phase lags as follows

$$\overline{\Delta\Phi} = \Delta\Phi(t_{\text{end}}) \tag{14}$$

$$\overline{\Delta\varphi_i} = \Delta\varphi_i(t_{\text{end}}) \tag{15}$$

Transient times

We defined the transient time t_S as the time to reach the steady-state overall phase lag $\overline{\Delta\Phi}$. For this purpose, the instantaneous overall phase lag over time $\Delta\Phi(t)$ was first smoothed with a moving average filter, and then t_S was measured arbitrarily as the time to reach within ±8% of $\overline{\Delta\Phi}$.

Statistical comparison of model configurations

The four model configurations in our robustness analysis were subject to gradual increases in the number of neural disruptions. We compared the forward swimming speed (= dependent variable) of these four configurations (= independent variable) at each number of neural disruptions separately by using a one-way ANOVA for independent samples ($n = 10$ for single-type neural disruptions and $n = 30$ for mixed neural disruptions; table S2). After verifying that the group mean swimming speeds were significantly different from the overall mean under a significance level of $P < 0.005$, we carried out a GH post hoc test (for unequal variances) to directly compare between the four model configurations. In each of these comparisons between the mean swimming performances, we used

independent samples. The P values along with a significance level of $P < 0.001$ were used to determine significant differences and a significance level of $P > 0.05$ to determine significant similarities between configurations.

We also carried out a comparison of the decline in robustness with increasing number of disruptions between the four configurations. For this purpose, we carried out ($n = 10$ for single type neural disruptions, $n = 30$ for mixed neural disruptions) linear regressions for each configuration and disruptions type. Subsequently, the mean slopes of these linear fits were statistically compared with a one-way ANOVA, followed by a GH post hoc test.

We report the P values in tables S2 and S3. All statistical tests were carried out using R (R Core Team, 2017) and the "userfriendlyscience" package.

Additional simulation experiments for the decoupled and oscillator-free configuration

Simulations to explore the effect of neural disruptions on swimming speed allowed us to systematically test a large number of randomly applied disruptions that would be too time consuming to carry out on the real robot. For the same reasons, to quantify the characteristics of the decoupled and oscillator-free configurations, we carried out a series of simulations to understand the effects of a few specific model parameters. We varied feedback strengths w_{fb} from 0 to 300 in steps of 25 for both cases. For the decoupled configuration, variable intrinsic frequencies in the range of 0.5 to 2 Hz in steps of 0.25 Hz were explored. In the oscillator-free configuration, overall central phase lags were varied from 0 to 200% in steps of 20% (with a corresponding uniform intersegmental phase lag bias ψ_{nj}). For both configurations, each parameter combination was simulated $n = 10$ times with a different random initialization of the oscillator phases φ_n. Following this simulation protocol, we carried out a total of 910 simulations for the decoupled case and 1430 simulations for the oscillator-free case. Each simulation lasted for a duration of 30 s to provide enough time to reach a steady-state swimming with a stable phase lag pattern along the body. The detailed results of these simulations are presented in figs. S4 and S6.

SUPPLEMENTARY MATERIALS

robotics.sciencemag.org/cgi/content/full/6/57/eabf6354/DC1
Supplementary Text S1 to S4
Figs. S1 to S6
Tables S1 to S3
Movies S1 to S4
References (*95–102*)

REFERENCES AND NOTES

1. T. G. Brown, On the nature of the fundamental activity of the nervous centres; together with an analysis of the conditioning of rhythmic activity in progression, and a theory of the evolution of function in the nervous system. *J. Physiol.* **48**, 18–46 (1914).
2. A. D. Kuo, The relative roles of feedforward and feedback in the control of rhythmic movements. *Motor Control* **6**, 129–145 (2002).
3. A. I. Selverston, Invertebrate central pattern generator circuits. *Philos. Trans. R. Soc. Lond. B Biol. Sci.* **365**, 2329–2345 (2010).
4. O. Kiehn, Decoding the organization of spinal circuits that control locomotion. *Nat. Rev. Neurosci.* **17**, 224–238 (2016).
5. S. Grillner, A. El Manira, Current principles of motor control, with special reference to vertebrate locomotion. *Physiol. Rev.* **100**, 271–320 (2020).
6. F. J. Eisenhart, T. W. Cacciatore, W. B. Kristan Jr., A central pattern generator underlies crawling in the medicinal leech. *J. Comp. Physiol. A* **186**, 631–643 (2000).
7. P. Wallén, T. L. Williams, Fictive locomotion in the lamprey spinal cord in vitro compared with swimming in the intact and spinal animal. *J. Physiol.* **347**, 225–239 (1984).
8. D. Ryczko, J. Knüsel, A. Crespi, S. Lamarque, A. Mathou, A. J. Ijspeert, J. M. Cabelguen, Flexibility of the axial central pattern generator network for locomotion in the salamander. *J. Neurophysiol.* **113**, 1921–1940 (2015).
9. A. E. Talpalar, J. Bouvier, L. Borgius, G. Fortin, A. Pierani, O. Kiehn, Dual-mode operation of neuronal networks involved in left-right alternation. *Nature* **500**, 85–88 (2013).
10. P. Wallén, Spinal mechanisms controlling locomotion in dogfish and lamprey. *Acta Physiol. Scand. Suppl.* **503**, 1–45 (1982).
11. A. D. McClellan, Locomotor recovery in spinal-transected lamprey: Regenerated spinal coordinating neurons and mechanosensory inputs couple locomotor activity across a spinal lesion. *Neuroscience* **35**, 675–685 (1990).
12. C. M. Rovainen, Synaptic interactions of identified nerve cells in the spinal cord of the sea lamprey. *J. Comp. Neurol.* **154**, 189–206 (1974).
13. S. Grillner, T. Williams, P. A. Lagerbäck, The edge cell, a possible intraspinal mechanoreceptor. *Science* **223**, 500–503 (1984).
14. G. V. Di Prisco, P. Wallén, S. Grillner, Synaptic effects of intraspinal stretch receptor neurons mediating movement-related feedback during locomotion. *Brain Res.* **530**, 161–166 (1990).
15. N. Massarelli, A. L. Yau, K. A. Hoffman, T. Kiemel, E. D. Tytell, Characterization of the encoding properties of intraspinal mechanosensory neurons in the lamprey. *J. Comp. Physiol. A Neuroethol. Sens. Neural Behav. Physiol.* **203**, 831–841 (2017).
16. S. Grillner, A. McClellan, C. Perret, Entrainment of the spinal pattern generators for swimming by mechano-sensitive elements in the lamprey spinal cord in vitro. *Brain Res.* **217**, 380–386 (1981).
17. E. D. Tytell, A. H. Cohen, Rostral versus caudal differences in mechanical entrainment of the lamprey central pattern generator for locomotion. *J. Neurophysiol.* **99**, 2408–2419 (2008).
18. J. Christenson, A. Boman, P. A. Lagerbäck, S. Grillner, The dorsal cell, one class of primary sensory neuron in the lamprey spinal cord. I. Touch, pressure but no nociception—A physiological study. *Brain Res.* **440**, 1–8 (1988).
19. A. R. Martin, W. O. Wickelgren, Sensory cells in the spinal cord of the sea lamprey. *J. Physiol.* **212**, 65–83 (1971).
20. J. T. Buchanan, A. H. Cohen, Activities of identified interneurons, motoneurons, and muscle fibers during fictive swimming in the lamprey and effects of reticulospinal and dorsal cell stimulation. *J. Neurophysiol.* **47**, 948–960 (1982).
21. E. D. Tytell, P. Holmes, A. H. Cohen, Spikes alone do not behavior make: Why neuroscience needs biomechanics. *Curr. Opin. Neurobiol.* **21**, 816–822 (2011).
22. A. J. Ijspeert, Biorobotics: Using robots to emulate and investigate agile locomotion. *Science* **346**, 196–203 (2014).
23. G. V. Lauder, E. J. Anderson, J. Tangorra, P. G. A. Madden, Fish biorobotics: Kinematics and hydrodynamics of self-propulsion. *J. Exp. Biol.* **210**, 2767–2780 (2007).
24. R. E. Ritzmann, R. D. Quinn, J. T. Watson, S. N. Zill, Insect walking and biorobotics: A relationship with mutual benefits. *Bioscience* **50**, 23–33 (2000).
25. L. Wen, Z. Ren, V. Di Santo, K. Hu, T. Yuan, T. Wang, G. V. Lauder, Understanding fish linear acceleration using an undulatory biorobotic model with soft fluidic elastomer actuated morphing median fins. *Soft Robot.* **5**, 375–388 (2018).
26. J. L. Tangorra, S. Naomi Davidson, I. W. Hunter, P. G. A. Madden, G. V. Lauder, H. Dong, M. Bozkurttas, R. Mittal, The development of a biologically inspired propulsor for unmanned underwater vehicles. *IEEE J. Ocean. Eng.* **32**, 533–550 (2007).
27. M. S. Triantafyllou, G. S. Triantafyllou, An efficient swimming machine. *Sci. Am.* **272**, 64–70 (1995).
28. J. Zhu, C. White, D. K. Wainwright, V. Di Santo, G. V. Lauder, H. Bart-Smith, Tuna robotics: A high-frequency experimental platform exploring the performance space of swimming fishes. *Sci. Robot.* **4**, eaax4615 (2019).
29. Z. Wolf, A. Jusufi, D. M. Vogt, G. V. Lauder, Fish-like aquatic propulsion studied using a pneumatically-actuated soft-robotic model. *Bioinspir. Biomim.* **15**, 04600 (2020).
30. S. Sefati, I. D. Neveln, E. Roth, T. R. T. Mitchell, J. B. Snyder, M. A. MacIver, E. S. Fortune, N. J. Cowan, Mutually opposing forces during locomotion can eliminate the tradeoff between maneuverability and stability. *Proc. Natl. Acad. Sci.* **110**, 18798–18803 (2013).
31. E. Kelasidi, P. Liljeback, K. Y. Pettersen, J. T. Gravdahl, Innovation in Underwater Robots: Biologically inspired swimming snake robots. *IEEE Robot. Autom. Mag.* **23**, 44–62 (2016).
32. B. Bayat, A. Crespi, A. Ijspeert, Envirobot: A bio-inspired environmental monitoring platform., in *Proceedings of the 2016 IEEE/OES Autonomous Underwater Vehicles (AUV)* (IEEE, 2016), pp. 381–386.
33. S. Hirose, M. Mori, H. Yamada, S. Chigisaki, ALL-N-020 Design and control of amphibous snake-like robot ACM-R5, in *Proceedings of JSME Annual Conference on Robotics and Mechatronics (Robomec)* (Japan Society of Mechanical Engineers, 2005), p. 9.
34. M. Rufo, M. Smithers, GhostSwimmer AUV: Applying biomimetics to underwater robotics for achievement of tactical relevance. *Mar. Technol. Soc. J.* **45**, 24–30 (2011).
35. D. Scaradozzi, G. Palmieri, D. Costa, A. Pinelli, BCF swimming locomotion for autonomous underwater robots: A review and a novel solution to improve control and efficiency. *Ocean Eng.* **130**, 437–453 (2017).
36. J. Ayers, *Architectures for Adaptive Behavior in Biomimetic Underwater Robots* (Bio-mechanisms of Swimming and Flying, Springer, 2004), pp. 171–187.

37. P. Arena, L. Fortuna, M. Frasca, G. Vagliasindi, A wave-based CNN generator for the control and actuation of a lamprey-like robot. *Intl. J. Bifurcat. Chaos* **16**, 39–46 (2006).
38. C. Stefanini, S. Orofino, L. Manfredi, S. Mintchev, S. Marrazza, T. Assaf, L. Capantini, E. Sinibaldi, S. Grillner, P. Wallén, P. Dario, A novel autonomous, bioinspired swimming robot developed by neuroscientists and bioengineers. *Bioinspir. Biomim.* **7**, 025001 (2012).
39. K. A. McIsaac, J. P. Ostrowski, Open-loop verification of motion planning for an underwater Eel-like robot, in *Experimental Robotics VII*, D. Rus, S. Singh, Eds. (Springer, 2001), pp. 271–280.
40. M. C. Leftwich, E. D. Tytell, A. H. Cohen, A. J. Smits, Wake structures behind a swimming robotic lamprey with a passively flexible tail. *J. Exp. Biol.* **215**, 416–425 (2012).
41. L. Manfredi, T. Assaf, S. Mintchev, S. Marrazza, L. Capantini, S. Orofino, L. Ascari, S. Grillner, P. Wallén, O. Ekeberg, C. Stefanini, P. Dario, A bioinspired autonomous swimming robot as a tool for studying goal-directed locomotion. *Biol. Cybern.* **107**, 513–527 (2013).
42. L. DeVries, F. D. Lagor, H. Lei, X. Tan, D. A. Paley, Distributed flow estimation and closed-loop control of an underwater vehicle with a multi-modal artificial lateral line. *Bioinspir. Biomim.* **10**, 025002 (2015).
43. A. Gao, M. Triantafyllou, Bio-inspired pressure sensing for active yaw control of underwater vehicles, in *Proceedings of the 2012 Oceans* (IEEE, 2012), pp. 1–7.
44. R. Venturelli, O. Akanyeti, F. Visentin, J. Ježov, L. D. Chambers, G. Toming, J. Brown, M. Kruusmaa, W. M. Megill, P. Fiorini, Hydrodynamic pressure sensing with an artificial lateral line in steady and unsteady flows. *Bioinspir. Biomim.* **7**, 036004 (2012).
45. T. Salumäe, M. Kruusmaa, Flow-relative control of an underwater robot. *Proc. R. Soc. A Math. Phys. Eng. Sci.* **469**, 20120671 (2013).
46. L. D. Chambers, O. Akanyeti, R. Venturelli, J. Ježov, J. Brown, M. Kruusmaa, P. Fiorini, W. M. Megill, A fish perspective: Detecting flow features while moving using an artificial lateral line in steady and unsteady flow. *J. R. Soc. Interface* **11**, 20140467 (2014).
47. M. Porez, F. Boyer, A. J. Ijspeert, Improved Lighthill fish swimming model for bio-inspired robots: Modeling, computational aspects and experimental comparisons. *Intl. J. Robot. Res.* **33**, 1322–1341 (2014).
48. F. Candelier, F. Boyer, A. Leroyer, Three-dimensional extension of Lighthill's large-amplitude elongated-body theory of fish locomotion. *J. Fluid Mech.* **674**, 196–226 (2011).
49. A. J. Ijspeert, A. Crespi, D. Ryczko, J.-M. Cabelguen, From swimming to walking with a salamander robot driven by a spinal cord model. *Science* **315**, 1416–1420 (2007).
50. N. Kopell, G. B. Ermentrout, Coupled oscillators and the design of central pattern generators. *Math. Biosci.* **90**, 87–109 (1988).
51. A. H. Cohen, G. B. Ermentrout, T. Kiemel, N. Kopell, K. A. Sigvardt, T. L. Williams, Modelling of intersegmental coordination in the lamprey central pattern generator for locomotion. *Trends Neurosci.* **15**, 434–438 (1992).
52. K. Matsuoka, Sustained oscillations generated by mutually inhibiting neurons with adaptation. *Biol. Cybern.* **52**, 367–376 (1985).
53. S. Knafo, K. Fidelin, A. Prendergast, P.-E. B. Tseng, A. Parrin, C. Dickey, U. L. Böhm, S. N. Figueiredo, O. Thouvenin, H. Pascal-Moussellard, C. Wyart, Mechanosensory neurons control the timing of spinal microcircuit selection during locomotion. *eLife* **6**, e25260 (2017).
54. S. Grillner, P. Wallén, L. Brodin, A. Lansner, Neuronal network generating locomotor behavior in lamprey: Circuitry, transmitters, membrane properties, and simulation. *Annu. Rev. Neurosci.* **14**, 169–199 (1991).
55. G. Daghfous, W. W. Green, S. T. Alford, B. S. Zielinski, R. Dubuc, Sensory activation of command cells for locomotion and modulatory mechanisms: Lessons from lampreys. *Front. Neural Circuits* **10**, 18 (2016).
56. S. Grillner, A. McClellan, K. Sigvardt, Mechanosensitive neurons in the spinal cord of the lamprey. *Brain Res.* **235**, 169–173 (1982).
57. L.-J. Hsu, P. V. Zelenin, S. Grillner, G. N. Orlovsky, T. G. Deliagina, Intraspinal stretch receptor neurons mediate different motor responses along the body in lamprey. *J. Comp. Neurol.* **521**, 3847–3862 (2013).
58. C. L. Hamlet, K. A. Hoffman, E. D. Tytell, L. J. Fauci, The role of curvature feedback in the energetics and dynamics of lamprey swimming: A closed-loop model. *PLOS Comput. Biol.* **14**, e1006324 (2018).
59. J. T. Buchanan, Contributions of identifiable neurons and neuron classes to lamprey vertebrate neurobiology. *Prog. Neurobiol.* **63**, 441–466 (2001).
60. C. Wyart, F. Del Bene, E. Warp, E. K. Scott, D. Trauner, H. Baier, E. Y. Isacoff, Optogenetic dissection of a behavioural module in the vertebrate spinal cord. *Nature* **461**, 407–410 (2009).
61. U. L. Böhm, A. Prendergast, L. Djenoune, S. Nunes Figueiredo, J. Gomez, C. Stokes, S. Kaiser, M. Suster, K. Kawakami, M. Charpentier, J.-P. Concordet, J.-P. Rio, F. Del Bene, C. Wyart, CSF-contacting neurons regulate locomotion by relaying mechanical stimuli to spinal circuits. *Nat. Commun.* **7**, 10866 (2016).
62. R. Dubuc, S. Grillner, The role of spinal cord inputs in modulating the activity of reticulospinal neurons during fictive locomotion in the lamprey. *Brain Res.* **483**, 196–200 (1989).
63. F. Brocard, D. Ryczko, K. Fénelon, R. Hatem, D. Gonzales, F. Auclair, R. Dubuc, The transformation of a unilateral locomotor command into a symmetrical bilateral activation in the brainstem. *J. Neurosci.* **30**, 523–533 (2010).
64. M. Antri, K. Fénelon, R. Dubuc, The contribution of synaptic inputs to sustained depolarizations in reticulospinal neurons. *J. Neurosci.* **29**, 1140–1151 (2009).
65. D. L. McLean, J. Fan, S.-I. Higashijima, M. E. Hale, J. R. Fetcho, A topographic map of recruitment in spinal cord. *Nature* **446**, 71–75 (2007).
66. K. Ampatzis, J. Song, J. Ausborn, A. El Manira, Separate microcircuit modules of distinct v2a interneurons and motoneurons control the speed of locomotion. *Neuron* **83**, 934–943 (2014).
67. S. Chevallier, M. Landry, F. Nagy, J.-M. Cabelguen, Recovery of bimodal locomotion in the spinal-transected salamander, *Pleurodeles waltlii*. *Eur. J. Neurosci.* **20**, 1995–2007 (2004).
68. G. Courtine, Y. Gerasimenko, R. van den Brand, A. Yew, P. Musienko, H. Zhong, B. Song, Y. Ao, R. M. Ichiyama, I. Lavrov, R. R. Roy, M. V. Sofroniew, V. R. Edgerton, Transformation of nonfunctional spinal circuits into functional states after the loss of brain input. *Nat. Neurosci.* **12**, 1333–1342 (2009).
69. P. E. Musienko, P. V. Zelenin, V. F. Lyalka, Y. P. Gerasimenko, G. N. Orlovsky, T. G. Deliagina, Spinal and supraspinal control of the direction of stepping during locomotion. *J. Neurosci.* **32**, 17442–17453 (2012).
70. A. Takeoka, I. Vollenweider, G. Courtine, S. Arber, Muscle spindle feedback directs locomotor recovery and circuit reorganization after spinal cord injury. *Cell* **159**, 1626–1639 (2014).
71. A. Frigon, The neural control of interlimb coordination during mammalian locomotion. *J. Neurophysiol.* **117**, 2224–2241 (2017).
72. J. C. Liao, Neuromuscular control of trout swimming in a vortex street: Implications for energy economy during the Kármán gait. *J. Exp. Biol.* **207**, 3495–3506 (2004).
73. D. N. Beal, F. S. Hover, M. S. Triantafyllou, J. C. Liao, G. V. Lauder, Passive propulsion in vortex wakes. *J. Fluid Mech.* **549**, 385 (2006).
74. M. Rubenstein, A. Cornejo, R. Nagpal, Programmable self-assembly in a thousand-robot swarm. *Science* **345**, 795–799 (2014).
75. S. Li, R. Batra, D. Brown, H.-D. Chang, N. Ranganathan, C. Hoberman, D. Rus, H. Lipson, Particle robotics based on statistical mechanics of loosely coupled components. *Nature* **567**, 361–365 (2019).
76. M. Yim, W.-M. Shen, B. Salemi, D. Rus, M. Moll, H. Lipson, E. Klavins, G. Chirikjian, Modular self-reconfigurable robot systems [Grand Challenges of Robotics]. *IEEE Robot. Autom. Mag.* **14**, 43–52 (2007).
77. S. Murata, E. Yoshida, A. Kamimura, H. Kurokawa, K. Tomita, S. Kokaji, M-TRAN: Self-reconfigurable modular robotic system. *IEEE/ASME Trans. Mechatron.* **7**, 431–441 (2002).
78. M. Dunbabin, L. Marques, Robots for environmental monitoring: Significant advancements and applications. *IEEE Robot. Autom. Mag.* **19**, 24–39 (2012).
79. S. Mintchev, C. Stefanini, A. Girin, S. Marrazza, S. Orofino, V. Lebastard, L. Manfredi, P. Dario, F. Boyer, An underwater reconfigurable robot with bioinspired electric sense, in *Proceedings of the 2012 IEEE International Conference on Robotics and Automation* (IEEE, 2012), pp. 1149–1154.
80. K. E. Peyer, L. Zhang, B. J. Nelson, Bio-inspired magnetic swimming microrobots for biomedical applications. *Nanoscale* **5**, 1259–1272 (2013).
81. A. Cully, J. Clune, D. Tarapore, J.-B. Mouret, Robots that can adapt like animals. *Nature* **521**, 503–507 (2015).
82. M. L. Visinsky, J. R. Cavallaro, I. D. Walker, Robotic fault detection and fault tolerance: A survey. *Reliab. Eng. Syst. Saf.* **46**, 139–158 (1994).
83. S. Grillner, T. Deliagina, A. El Manira, R. H. Hill, Neural networks that co-ordinate locomotion and body orientation in lamprey. *Trends Neurosci.* **18**, 270–279 (1995).
84. A. Crespi, K. Karakasiliotis, A. Guignard, A. J. Ijspeert, Salamandra Robotica II: An amphibious robot to study salamander-like swimming and walking gaits. *IEEE Trans. Robot.* **29**, 308–320 (2013).
85. I. Youssef, M. Mutlu, B. Bayat, A. Crespi, S. Hauser, J. Conradt, A. Bernardino, A. Ijspeert, A neuro-inspired computational model for a visually guided robotic lamprey using frame and event based cameras. *IEEE Robot. Autom. Lett.* **5**, 2395–2402 (2020).
86. D. Korkmaz, G. O. Koca, G. Li, C. Bal, M. Ay, Z. H. Akpolat, Locomotion control of a biomimetic robotic fish based on closed loop sensory feedback CPG model. *J. Marine Eng. Technol.* **20**, 125–137 (2021).
87. Ö. Ekeberg, S. Grillner, A. Lansner, The neural control of fish swimming studied through numerical simulations. *Adapt. Behav.* **3**, 363–384 (1995).
88. Y. Xu, K. Mohseni, A pressure sensory system inspired by the fish lateral line: Hydrodynamic force estimation and wall detection. *IEEE J. Oceanic Eng.* **42**, 532–543 (2017).
89. J. Jezov, O. Akanyeti, L. D. Chambers, M. Kruusmaa, Sensing oscillations in unsteady flow for better robotic swimming efficiency, in *Proceedings of the 2012 IEEE International Conference on Systems, Man, and Cybernetics (SMC)* (IEEE, 2012), pp. 91-96.
90. Ö. Ekeberg, A combined neuronal and mechanical model of fish swimming. *Biol. Cybern.* **69**, 363–374 (1993).

91. R. H. Myers, D. C. Montgomery, C. M. Anderson-Cook, *Response Surface Methodology: Process and Product Optimization Using Designed Experiments* (John Wiley & Sons, 2016).
92. M. J. Lighthill, Large-amplitude elongated-body theory of fish locomotion. *Proc. R. Soc. Lond. B Biol. Sci.* **179**, 125–138 (1971).
93. B. Mirtich, Fast and accurate computation of polyhedral mass properties. *J. Graphics Tools* **1**, 31–50 (1996).
94. K. Matsuoka, Analysis of a neural oscillator. *Biol. Cybern.* **104**, 297–304 (2011).
95. F. Boyer, M. Porez, A. Leroyer, M. Visonneau, Fast dynamics of an eel-like robot—Comparisons with navier–stokes simulations. *IEEE Trans. Robot.* **24**, 1274–1288 (2008).
96. M. Gazzola, M. Argentina, L. Mahadevan, Gait and speed selection in slender inertial swimmers. *Proc. Natl. Acad. Sci. U.S.A.* **112**, 3874–3879 (2015).
97. E. M. Izhikevich, *Dynamical Systems in Neuroscience* (MIT Press, 2007).
98. Y. Kuramoto, *Chemical Oscillations, Waves, and Turbulence* (Springer Series in Synergetics, Springer, 1984).
99. M. J. Lighthill, Aquatic animal propulsion of high hydromechanical efficiency. *J. Fluid Mech.* **44**, 265–301 (1970).
100. D. Owaki, T. Kano, K. Nagasawa, A. Tero, A. Ishiguro, Simple robot suggests physical interlimb communication is essential for quadruped walking. *J. R. Soc. Interface* **10**, 20120669 (2013).
101. A. Pikovsky, M. Rosenblum, J. Kurths, *Synchronization: A Universal Concept in Nonlinear Science* (Cambridge Univ. Press, 2002), vol. 12.
102. A. T. Winfree, Biological rhythms and the behavior of populations of coupled oscillators. *J. Theor. Biol.* **16**, 15–42 (1967).

Acknowledgments: We thank A.Crespi, J. Knuesel, T. Horvat, B. Bayat, A. Petitjean, and F. Dzeladini for technical support; A. Oates for suggesting to investigate neural disruptions; and E. Standen and K. Lutek for valuable feedback. **Funding:** R.T. was supported by the Swiss National Science Foundation (SNSF); K.M. was supported by KM-RoBoTa; L.P. and A.J.I. were supported by NCCR Robotics. L.P., K.A., T.K., A.I., and A.J.I. were supported by the Human Frontier Science Program (grant RGP0027/2017). D.R. was supported by the Natural Sciences and Engineering Research Council of Canada (NSERC), Fonds de Recherche en Santé du Québec (FRQS), and Canadian Institutes of Health Research (CIHR). **Author contributions:** R.T., A.I., and A.J.I. conceived the study. R.T., A.I., A.J.I., T.K., and K.M. designed the feedback entrainment mechanism. K.M. designed the robot. L.P. designed the sensor units. L.P. and R.T. programmed the robot. R.T. designed and carried out the simulations. L.P. and K.M. designed and carried out the experiments with the robot. R.T., K.M. and L.P. analyzed the data. K.A. and R.T. implemented and tested the Matsuoka network model. J.H. and F.B. performed the theoretical analysis. K.M. created the interactive website. R.T., K.M., D.R., and A.J.I. wrote the manuscript. All authors contributed to and approved the final draft of the manuscript. **Competing interests:** The authors declare that they have no competing interests. **Data and materials availability:** Our results can be explored on the interactive data visualization website: https://go.epfl.ch/AgnathaX. Data and code that support the findings of this study are available on https://doi.org/10.6084/m9.figshare.c.5535195. Simulation code is available at https://gitlab.com/robintha/agnathax-simulation.

Submitted 9 November 2020
Accepted 21 July 2021
Published 11 August 2021
10.1126/scirobotics.abf6354

Citation: R. Thandiackal, K. Melo, L. Paez, J. Herault, T. Kano, K. Akiyama, F. Boyer, D. Ryczko, A. Ishiguro, A. J. Ijspeert, Emergence of robust self-organized undulatory swimming based on local hydrodynamic force sensing. *Sci. Robot.* **6**, eabf6354 (2021).

Science Robotics

Emergence of robust self-organized undulatory swimming based on local hydrodynamic force sensing

Robin Thandiackal, Kamilo Melo, Laura Paez, Johann Herault, Takeshi Kano, Kyoichi Akiyama, Frédéric Boyer, Dimitri Ryczko, Akio Ishiguro, and Auke J. Ijspeert

Sci. Robot. **6** (57), eabf6354. DOI: 10.1126/scirobotics.abf6354

Science Robotics (ISSN 2470-9476) is published by the American Association for the Advancement of Science. 1200 New York Avenue NW, Washington, DC 20005. The title *Science Robotics* is a registered trademark of AAAS.